

2017

Experimental Validation of Finite Element Predicted Bone Strain in the Human Metatarsal

Fung, Anita

Fung, A. (2017). Experimental Validation of Finite Element Predicted Bone Strain in the Human Metatarsal (Master's thesis, University of Calgary, Calgary, Canada). Retrieved from <https://prism.ucalgary.ca>. doi:10.11575/PRISM/26071

<http://hdl.handle.net/11023/3715>

Downloaded from PRISM Repository, University of Calgary

UNIVERSITY OF CALGARY

Experimental Validation of Finite Element Predicted Bone Strain in the Human
Metatarsal

by

Anita Fung

A THESIS

SUBMITTED TO THE FACULTY OF GRADUATE STUDIES
IN PARTIAL FULFILMENT OF THE REQUIREMENTS FOR THE
DEGREE OF MASTER OF SCIENCE

GRADUATE PROGRAM IN BIOMEDICAL ENGINEERING

CALGARY, ALBERTA

APRIL, 2017

© Anita Fung 2017

Abstract

The objective of this study was to verify and validate a finite element modeling routine for the human metatarsal, which is a common location for stress fractures. Experimental strain measurements on 33 human cadaveric metatarsals subject to cantilever bending were compared with strain predictions from finite element (FE) models generated from computed tomography images. For the material property assignment of the FE models, a published density-elasticity relationship was compared with density-elasticity equations developed using optimization techniques. The correlations between the measured and predicted and predicted strains were very high ($r^2 \geq 0.94$) for all of the density-elasticity equations. However, the utilization of an optimized density-elasticity equation improved the accuracy of the finite element models, reducing the maximum error between measured and predicted strains by 10% to 20%. The finite element modeling routine could be used for investigating potential interventions to minimize metatarsal strains and the occurrence of metatarsal stress fractures.

Acknowledgements

None of my major accomplishments were ever done without help from others, and this project was no different. Firstly, I would like to thank the Biomedical Engineering Graduate Program and NSERC, which had both made this research possible.

I must acknowledge my supervisory committee, Dr. Tannin Schmidt and Dr. Steven Boyd, for their time, effort, and helpful advice during the course of my project. Also, I would like to thank the other members of my examination committee, Dr. Leping Li and Dr. Preston Wiley, for their excellent feedback on my thesis.

I am indebted to Lindsay Loundagin for all of her help on this project. She had taken an immense amount of time out of her busy schedule to not only assist with the mechanical testing, but also to attend the CT scanning sessions at the other campus, and to dissect the cadavers.

I must also acknowledge Mehdi Shekarforoush for his assistance with the digitization, Majid Nazemi for his advice on the optimization routine, Stephanie Kwong for imaging the cadavers, and the Body Donation Program for providing the cadavers. A special mention goes out to my dad for chauffeuring the dismembered feet between the campuses.

Many people have spent several hours helping me organize my presentations for my seminar and defense. I would like to thank Ifaz Haider for his time and patience, as he

had sat through no less than three versions of my presentation and provided very helpful feedback on every slide. I am also grateful for the help provided by Dr. Art Kuo and the Neuromechanics group, as they had spent several hours providing useful feedback and discussing ways to improve my presentation.

I have enjoyed working in this lab, and I would like to thank my fellow lab members over the years, Lindsay, Colin, Aleen, Olivia, Michael, and Ifaz, along with my fellow office detainees, Alissa, Emily, Niki, and Kaleena, for their friendship, advice, and encouragement. Their kindness, insight, and humour had helped make even the most challenging phases of my graduate journey more enjoyable.

I would like to thank my older brothers, Byron and Leo, for their positive influence since the beginning. Their success had set good examples for me to follow, and they inspired me to stay on the right track during my studies.

I would like to express my appreciation for my parents, who are tremendous role models and have provided an immeasurable amount of support. Their hard work had helped me become a better person, and had allowed me to dream big.

Finally, I would like to thank my supervisor, Dr. Brent Edwards, who has been my mentor and research advisor since my undergraduate years. Brent had spent countless hours helping me become a better researcher. The lab he has set up has become a launching pad for many exciting journeys. I could not have asked for a better advisor.

For my parents, who had taken me on weekly trips to the library all those years ago.

Table of Contents

ABSTRACT.....	II
ACKNOWLEDGEMENTS	III
TABLE OF CONTENTS.....	VI
LIST OF TABLES	VIII
LIST OF FIGURES	IX
LIST OF SYMBOLS, ABBREVIATIONS AND NOMENCLATURE	XI
CHAPTER ONE: INTRODUCTION.....	1
1.1 Thesis Objective.....	1
1.2 Hypothesis.....	1
1.3 Thesis Outline	2
CHAPTER TWO: LITERATURE REVIEW.....	4
2.1 Stress Fractures	4
2.1.1 Extrinsic Risk Factors.....	4
2.1.2 Intrinsic Risk Factors.....	6
2.2 Bone Biology	9
2.3 Mechanical Behaviour of Cortical Bone	13
2.4 Mechanical Behaviour of Trabecular Bone	15
2.5 Bone Damage and Repair	16
2.6 Stress Fracture Pathophysiology.....	17
2.7 Metatarsal Stress Fractures	18
2.8 <i>In Vivo</i> Bone Strain Measurement	19
2.8.1 Direct Strain Gauge Attachment	20
2.8.2 Bone Staples with Strain Gauges	21
2.8.3 In vivo Metatarsal Strain Results	22
2.8.4 Limitations of <i>in vivo</i> Measurement.....	22
2.9 The Finite Element Method	23
2.9.1 Verification and Validation of Finite Element Models	25
2.10 Summary of Literature Review.....	27
CHAPTER THREE: EXPERIMENTAL VALIDATION OF FINITE ELEMENT PREDICTED BONE STRAIN IN THE HUMAN METATARSAL	28
3.1 Abstract.....	29
3.2 Introduction.....	30
3.3 Methods	32
3.3.1 Specimens.....	32
3.3.2 Imaging Acquisition	32

3.3.3 Mechanical Testing	34
3.3.4 Finite Element Modeling.....	35
3.3.5 Density-Elasticity Equations and Optimization	38
3.3.6 Data Reduction and Statistical Analysis.....	42
3.4 Results.....	43
3.4.1 Experimental Strain Measurements.....	43
3.4.2 Published Density-Elasticity Equation	43
3.4.3 Optimized Single Density-Elasticity Equation.....	44
3.4.4 Optimized Piecewise Density-Elasticity Equation.....	46
3.5 Discussion.....	47
3.6 Conclusions.....	50
3.7 Acknowledgements.....	50
 CHAPTER FOUR: CONCLUSION.....	 51
4.1 Summary of Study	51
4.2 Study Limitations.....	52
4.3 Future Directions	56
4.4 Final Remarks	58
 REFERENCES	 60
 APPENDIX A : CROSS-VALIDATION OF FE-PREDICTED METATARSAL STRAINS SUGGESTS AN INFLUENCE OF AGE AND VBMD ON DENSITY-ELASTICITY RELATIONSHIPS	 88
 APPENDIX B : THE EFFECT OF LOADING ANGLE ON THE VALIDITY OF THE DENSITY-ELASTICITY RELATIONSHIP IN A FINITE ELEMENT MODEL	 91
 APPENDIX C: COPYRIGHT PERMISSIONS	 95

List of Tables

Table 3-1. Cadaver demographic information.....	32
Table 3-2. Validation parameters for the training and test sets as a function of published and optimized density-elasticity equations.....	44
Table A-1. Slope, intercept, correlation, R^2 , RMSE in microstrain and as a percentage of the peak measured strain, and maximum error in microstrain and as a percentage of the peak measured strain for different sets of models created using the published density-elasticity equation, $E = 0.51\rho_{app}^{1.37}$ (1).....	89
Table B-1. Slope, intercept, correlation, R^2 , RMSE in microstrain and as a percentage of the peak measured strain, and maximum error in microstrain and as a percentage of the peak measured strain for different metatarsal angles relative to the horizontal axis. All models were created using the published density- elasticity equation, $E = 0.51\rho_{app}^{1.37}$ (3).....	92

List of Figures

- Figure 2-1. Transmission electron micrograph of decalcified woven bone matrix displaying characteristic irregular orientation of collagen fibres. Image by Robert M. Hunt, 2011. Public domain. Retrieved from https://en.wikipedia.org/wiki/File:Woven_bone_matrix.jpg10
- Figure 2-2. Microscopic structure of bone. Image by U.S. National Cancer Institute's Surveillance, Epidemiology and End Results (SEER) Program, 2011. Public domain. Retrieved from Wikimedia Commons: https://en.wikipedia.org/wiki/File:Illu_compact_spongy_bone.jpg12
- Figure 2-3. Transverse view of the bones in the right foot. Metatarsal bones are shown in purple. Image by Henry Vandyke Carter, 1858. Public domain. Retrieved from Wikimedia Commons: <https://commons.wikimedia.org/wiki/File:Gray268.png>19
- Figure 2-4. Medial X-ray view of instrumented staple inserted in the second metatarsal (7). Used with permission.....22
- Figure 3-1. Sagittal (top left) and transverse (bottom left) views of a representative CT scan. Lines A and B depict the location of the proximal (top right, A) and distal (bottom right, B) frontal views of the metatarsals. The calibration phantom is visible in the sagittal and frontal views along with the wooden jig used to align the foot during scanning.....33

Figure 3-2. Photo of a representative experimental test set-up. A displacement/force was applied to the plantar surface of the metatarsal (denoted by arrow F) while the metatarsal was positioned at angle θ in the aluminum pot. Periosteal strain gauges are visible on the dorsal surface of the diaphysis.35

Figure 3-3. a) Representative cross-sectional view of the elastic modulus distribution for the published density-elasticity equation (187) and b) FE-predicted minimum principal strain distribution for a second metatarsal loaded in cantilever bending.....37

Figure 3-4. Measured vs. predicted principal strains at 25 N for metatarsals using the published equation: a) training set, and b) test set; optimized single equation: c) training set, and d) test set; and optimized piecewise equations: e) training set, and f) test set.45

Figure 3-5. Elastic modulus vs. apparent density for the published and optimized density-elasticity equations.46

Figure A-1. Measured vs. predicted strains for all metatarsals using the published density-elasticity equation, $E = 0.51\rho_{app}^{1.37}$ (1).....88

Figure A-2. Measured vs. predicted strains for metatarsals with a higher vBMD (0.40-0.73 g/cm³, black markers), and lower vBMD (0.15-0.34 g/cm³, grey markers) using the published density-elasticity equation, $E = 0.51\rho_{app}^{1.37}$ (1)89

List of Symbols, Abbreviations and Nomenclature

Symbol	Definition
BMD	Bone Mineral Density
CT	Computed Tomography
FE	Finite Element
MIL	Mean Intercept Length
MRI	Magnetic Resonance Imaging
vBMD	Volumetric Bone Mineral Density
$\mu\epsilon$	Microstrain (10^{-6} strain)

Chapter One: INTRODUCTION

Stress fractures are common overuse injuries among physically active individuals making up some 10% of all athletic injuries (1) and 31% of injuries in the military (2). One of the most common locations for stress fractures is the metatarsal bones of the foot, which account for 10%-20% of all stress fractures (3). Stress fractures are associated with the mechanical fatigue of bone, or the progressive loss of stiffness and strength of a material subject to repetitive loading. Mechanical fatigue is highly dependent on the resulting strains from the applied loads (4). As the *in vivo* measurement of bone strain is highly invasive and limited to small, localized regions of the bone surface (5–7), computational approaches such as the finite element (FE) method have become increasingly important for strain estimation (8,9).

1.1 Thesis Objective

The objective of this thesis was to verify and validate a subject-specific finite element modeling routine for strain estimation in the human metatarsal.

1.2 Hypothesis

Finite element models using optimized density-elasticity relationships would provide more accurate metatarsal strain predictions than finite element models using a published density-elasticity relationship.

1.3 Thesis Outline

This thesis contains four chapters.

Chapter 1 provides a brief overview of the research topic and outlines the structure of the thesis.

Chapter 2 provides a comprehensive literature review of topics related to this thesis, including background information relating to stress fractures, the mechanics of bone, *in vivo* strain measurement, and finite element modeling.

Chapter 3 is a manuscript submitted for publication to the Journal of Biomechanics entitled “Experimental Validation of Finite Element Predicted Bone Strain in the Human Metatarsal”. This study was the main focus of the thesis. Data collection was performed by Anita Fung and Lindsay Loundagin. All data analysis was performed by Anita Fung. This work was done under the supervision of Dr. W. Brent Edwards and the advisement of Dr. Tannin Schmidt and Dr. Steven Boyd.

Chapter 4 presents conclusions, limitations, and future directions based on Chapter 3.

Appendix A takes a closer examination of the FE strain predictions from the models using the published density-elasticity equations. The section suggests reasons why the FE

predictions for metatarsals with lower volumetric bone mineral density (vBMD) were less accurate than for the metatarsals with higher vBMD.

Appendix B describes the results of a concurrent study examining the influence of metatarsal loading angle on the validity of a density-elasticity relationship of a finite element model. The results showed that the FE strain predictions using the published density-elasticity equation were more accurate when the metatarsals were positioned more vertically.

Chapter Two: LITERATURE REVIEW

2.1 Stress Fractures

A stress fracture is a partial or complete fracture of the bone associated with repetitive loading at magnitudes below those which would normally result in a fracture under a monotonic load (10). The loads acting on the skeleton include contractile muscle forces, joint reaction forces, and forces external to the body (11). When these loads are continuously applied without allowing the bones to repair and adapt, stress fractures may occur. Stress fractures typically affect physically active individuals taking part in almost all athletic activities, as well as military recruits (11). The incidence of stress fractures have been reported to represent 10% of athletic injuries in a study of 320 cases (1), and 5% of all injuries experienced by military recruits (11). From an epidemiological perspective, risk factors for stress fracture may be described as being either extrinsic and intrinsic to the individual.

2.1.1 Extrinsic Risk Factors

Extrinsic risk factors are related to the training or competing environment where stress fractures occur. The occurrence of stress fractures is reported to be correlated to a higher weekly running mileage (12), as well as higher intensities and frequencies of training in both the military (13,14) and professional sports teams (15). As the training intensity is decreased, the loads on the bone are decreased, so bone damage is less likely to manifest. There is also more time for any damaged bone to be repaired, and for any new bone

resulting from the bone's repair process to become fully mineralized. Thus, in low intensity training scenarios it is expected that the bone is sufficiently strong enough to withstand the loads it experiences.

Footwear older than 6 months has been attributed to a higher risk of stress fractures (16). As the shoe sustains damage during use, the material becomes less capable of attenuating the dynamic loads that are transferred through the shoe. Therefore, with older shoes, higher loads would be transmitted to the bone, which increases the risk of stress fracture.

The literature presents varying results on the influence of training surfaces on the risk of stress fractures. This is likely, in part, because of difficulties in controlling for and quantifying training surfaces and terrains (16,17). Several studies have found no effect of training surface on the risk of stress fractures (12,18,19), while others have shown a correlation (20–22). While harder surfaces may cause a higher load to be transferred to the bone during impact, more compliant surfaces requires a greater energy expenditure, which hastens the onset of muscle fatigue and would also increase the risk of stress fractures (17).

The type of activity also influences the risk of stress fractures. Sprinters, hurdlers, and jumpers are reported to have a higher risk of stress fractures in the foot, as large forces are involved at the heel and metatarsal heads in these activities (16,17). On the other hand, middle and long distance runners are more likely to suffer from stress fractures of the pelvis or the long bones of the lower limb (16,17). Non-weight bearing bones could

also be susceptible to stress fractures depending on the activity. Baseball pitchers are at a higher risk of midshaft humeral stress fractures, as this site is loaded repetitively during throwing (23). Similarly, rowers and golfers are at a higher risk of stress fractures in the rib (24–26).

2.1.2 Intrinsic Risk Factors

For uniaxial loads, bones with a larger cross-sectional area can withstand higher loads prior to failure. In bending and torsional loads, the cross-sectional area and the cross-sectional moments of inertia have an influence on the bending stresses. Bone tissue further from the neutral axis is subject to higher stresses during bending and torsion, and is thus stronger and more adapted to higher loads (10). Prospective studies on military recruits have found that trainees who had sustained stress fractures had a smaller tibial width, cross-sectional area, and moment of inertia than those who did not have injuries (27).

Skeletal muscle may contribute to both the risk and prevention of stress fractures, depending on the site of injury (28). Some investigators believe that muscles produce large strains in bone, especially at the muscle attachment points (29). This could potentially contribute to the occurrence of stress fractures in the upper body, such as at the ribs during rowing (25) and golfing (24), or in the humerus during throwing (23). However, during the dynamic loading of weight-bearing bones, the contraction of muscles could attenuate loads and lower bending strains of long bones (7,30,31). Using a

musculoskeletal model, Scott and Winter (32) showed that ground reaction forces during running cause a bending moment, which is reduced by the contraction of the calf muscles. Studies measuring the circumference of the calf (33,34) while accounting for skinfold thickness have found that individuals with a larger calf circumference had a reduced likelihood of developing tibial stress fractures. Tibial bone width was also found to be independent of the calf circumference (34). This indicates that the muscles tend to attenuate loads in the lower extremity. It follows that as muscles become weaker at the onset of muscle fatigue, the ability of the muscles to absorb the loads decreases, and subsequently, a larger portion of the load is transferred to the bone. Thus, the occurrence of stress fractures may be more likely due to the higher loads imposed on the bone as muscles become weaker.

Studies on the military have shown that females are 3.5 to 10 times more likely to sustain stress fractures than their male counterparts (11,35). The difference in injury risk between males and females are less pronounced in athletic populations (33), although this may be due to difficulties in controlling the amount and intensity of training undergone by males and females. As females and males in military training are typically required to carry similar weight packs, the differences observed in military recruits could be due to narrower bone width which are less adapted to high loads (36). Another possible explanation for the higher incidence of stress fractures in female military recruits could be a slower rate of muscle force development in females (37,38), which inhibits the muscles' ability to attenuate loads.

Inadequate dietary intake, exhibited by eating disorders such as anorexia nervosa, is also suggested to be a risk factor in developing stress fractures. Anorexia nervosa has been associated with a lower bone mineral density (BMD). Bones with lower BMD are less stiff and subsequently experience higher strains than denser bones (39). As strain magnitudes highly influence the fatigue life of bone (4) and stress fractures are hypothesized to be related to mechanical fatigue (4,40), it follows that individuals with anorexia nervosa have a higher risk of developing stress fractures (41,42).

Furthermore, an imbalance of reproductive hormones could also be a risk factor for developing stress fractures. Menstrual disturbances in female athletes are usually indicative of lower basal estrogen concentrations compared to female athletes without menstrual disturbances (43). It is hypothesized that estrogen deficiencies change the mechanical stimulus threshold for bone remodeling, which makes the bone less likely to adapt to increased loading (44,45). This leads to a reduction in BMD (46) which increases the risk of stress fractures, as discussed previously. Studies examining the effect of reduced testosterone levels in male athletes have not observed a reduced BMD (47,48).

The results from studies examining the influence of age on stress fracture risk have been inconsistent. Some studies have found an increased risk of stress fractures with increasing age (49), while other studies have found a decreased risk of stress fractures (15) or no effect (50). The lack of agreement between the different studies could be caused by confounding factors such as the previous physical activity level.

The previous physical activity level of military recruits was assessed using a survey questionnaires and fitness tests in previous studies (33,49). The stress fracture risk was higher for individuals who were most sedentary and least fit prior to entering the armed forces. This may be because the musculoskeletal system of such individuals is less adapted to the physical demands of the training program. Regardless of the epidemiology, stress fractures are overuse injuries that manifests at the bone tissue level. Thus, an understanding of basic bone biology is necessary to explain the causes of stress fractures.

2.2 Bone Biology

The functions of bones are to provide mechanical support, store minerals such as calcium, provide a site for blood cell production, and enable mobility (51). The major components of bone are hydroxyapatite mineral, type I collagen fibrils, and water (52). The hydroxyapatite crystals are responsible for the compressive strength of the bone (16) and form thin plates, which are approximately $50 \times 25 \times 0.2$ nm in size. The orientation of the hydroxyapatite crystals is partially responsible for the anisotropy of the bone's mechanical properties (53). The thin plates of hydroxyapatite are arranged in layers in the three-dimensional arrays formed by collagen fibrils (52,54). The collagen fibrils are 80-100 nm in diameter, and are organized in a protein matrix called an osteoid (55). The collagen orientation within the osteoid influences the bone's mechanical properties (56,57) and provides tensile strength (16) and ductility (58). Water fills the gaps in the mineralized collagen matrix, and also within the collagen fibril (52). The presence of water extends the fatigue life and toughness of bone, but decreases the elastic modulus

and strength (59–61). Water also plays a role in the viscoelastic behaviour of bone (62). Other components, which make up a small proportion of the bone composition, include proteoglycans, matrix proteins, growth factors, and cytokines (16).

At the microscopic level, there are two types of bone: woven and lamellar. Woven bone is highly mineralized and contains randomly-oriented, fine-fibred collagen which is not aligned with stress patterns. It is rapidly formed during development and after a fracture (16,52), and has lower mechanical strength than lamellar bone (63). The woven bone formed during development is replaced by lamellar bone by 4 years of age (16). The collagen fibres of lamellar bone are thicker, laid down more slowly, and are aligned in a characteristic direction (64).

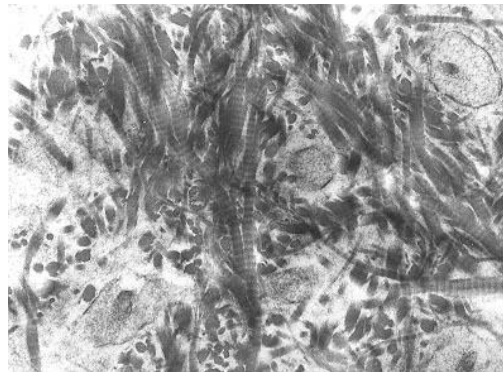


Figure 2-1. Transmission electron micrograph of decalcified woven bone matrix displaying characteristic irregular orientation of collagen fibres. Image by Robert M. Hunt, 2011. Public domain. Retrieved from https://en.wikipedia.org/wiki/File:Woven_bone_matrix.jpg

At the macroscopic level, bone has two subtypes: cortical and trabecular bone. The denser cortical bone is found primarily at the diaphysis and outer surface of bones, where stress fractures are more likely to occur (16). Cortical bone can be further differentiated between primary and secondary bone. Primary bone is the first bone formed in a given region, and can consist of circumferential lamellar bone or woven-fibred bone (65). The circumferential lamellar bone is a layered structure that surrounds a cylindrical canal, which contain blood vessels or nerves. The resulting cylindrical bone tissue is surrounded by the woven-fibred bone, and these units are called primary Haversian systems, or primary osteons (65). On the other hand, secondary bone is deposited after the removal of previously-formed bone, and consists of circumferential lamellar tissue. Unlike primary osteons, the secondary osteons are bounded by cement lines, which are thin areas, less than a few microns thick, of collagen-deficient bone. Cement lines are the result of the activity of cells which resorb and deposit the bone tissue (66), and are thought to be responsible for the weaker material properties of secondary bone compared to primary bone (67–69). Cement lines have also been hypothesized to play a role in preventing the propagation of fatigue microcracks (70).

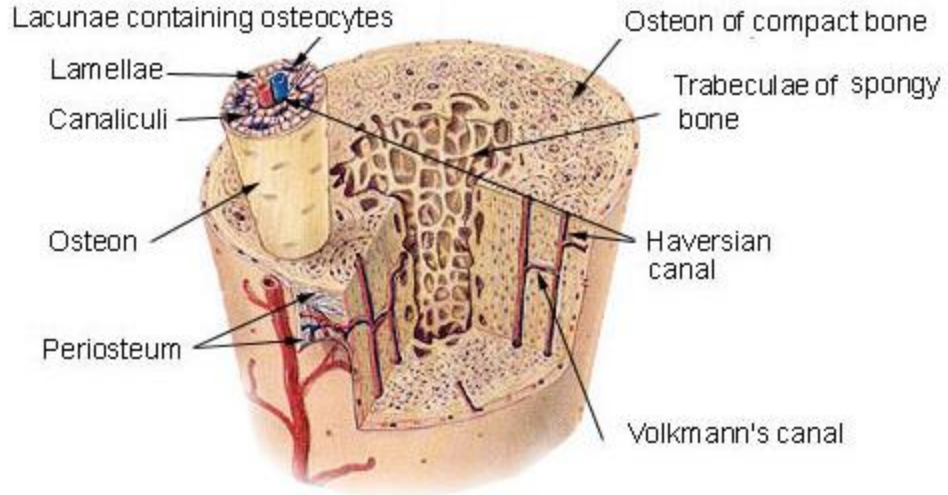


Figure 2-2. Microscopic structure of bone. Image by U.S. National Cancer Institute's Surveillance, Epidemiology and End Results (SEER) Program, 2011. Public domain.

Retrieved from Wikimedia Commons:

https://en.wikipedia.org/wiki/File:Illu_compact_spongy_bone.jpg

Trabecular bone has a higher porosity when compared to cortical bone, and is found primarily in the metaphysis region of bones. In living bone, the pores and spaces within the trabecular bone are filled with marrow and blood vessels (16,71).

Bone is formed by cells called osteoblasts, which produce the bone matrix. As osteoblasts mature, they become surrounded by the bone matrix and turn into osteocytes. Osteocytes produce components that maintain the extracellular concentration of ions (16). It is also believed that osteocytes detect changes in stimulus and orchestrate a bone adaptation response (72), although little direct evidence of such signaling have been found (73). The third major cell found in bone is the osteoclast, which is responsible for resorbing bone

by releasing enzymes and ions that dissolve the hydroxyapatite and digest the collagen (16).

2.3 Mechanical Behaviour of Cortical Bone

Cortical bone has anisotropic material properties, which means that its strength and elastic properties are direction-dependent. In addition, the mechanical properties of cortical bone are also asymmetric, which means it is stronger in compression than in tension. The ultimate strength and strain of cortical bone decreases with age (74) as porosity increases (75). The loss of bone density associated with aging also decreases the energy absorption capacity of cortical bone, which leads to more brittle behaviour and an increase in fracture risk (75–78). Increased porosity is also correlated with other microstructural changes that weaken cortical bone, such as an increase in osteon number, cement lines, and secondary bone (75).

In terms of microstructure effects, primary bone is stronger and more fatigue-resistant than secondary bone (79–82). However, information on the mechanical properties of lamellar bone is sparse (83), and those for woven bone have not been measured (65) due to experimental limitations. Nevertheless, clinical evidence suggests that the random orientation of the collagen fibres in woven bone is detrimental for bone strength (84).

Studies performed on single osteons show that transversely-oriented collagen fibres increase the compressive strength and modulus of the bone, while longitudinally-oriented

fibres increase the tensile strength and modulus (85–87). The cross-link density in the collagen fibres also affect the mechanical properties of the bone. Increased cross-linking is associated with increased mineralization, as well as stiffening of the collagen matrix itself (88). The number of cross-links increase with age, which could decrease the amount of energy absorbed prior to fracture, and cause the bone to become more brittle (89,90).

Cortical bone also exhibits small but significant viscoelastic behaviour. When the strain rate is increased by 6 orders of magnitude, strength and modulus increase by a factor of 3 (74). Modulus, strength, and toughness are slightly higher at higher strain rates. A ductile-to-brittle transition may exist in which the fracture toughness and energy absorption starts to decrease when the strain rate is higher than a threshold (91). As physiological strain rates have a relatively narrow range of 0.01%-1% s^{-1} , cortical bone can be assumed to have negligible strain rate effects in monotonic loading within the physiological range (69,74,92–94).

Experiments involving double-notched bone specimens undergoing four-point bending (95) have shown that cortical bone fails at the areas of highest strains at the root of the notch. This differs from the behavior of brittle engineering materials, which would fail at the elastic-plastic interface ahead of the notch, which is the area of the highest local stresses (96). Thus, strain has a higher influence on the failure of bone than stress (95).

At loads beyond the yield point, cortical bone exhibits mechanical property degradation (97,98). Mechanical property degradation and damage accumulation of cortical bone is

also caused by mechanical fatigue (99). Creep deformation, which is the permanent deformation under a sustained sub-maximal load, also contributes to the damage (99). Damage due to creep appears to have a synergistic effect with the damage due to mechanical fatigue. This is illustrated by the results of tests performed by Caler and Carter (99), which showed that cortical bone loaded in cyclic tension-compression tests exhibit a shorter fatigue life than it would if the effects of cycle-dependent and time-dependent damage were simply added.

2.4 Mechanical Behaviour of Trabecular Bone

Compared to cortical bone, the mechanical properties of trabecular bone are more difficult to measure due to heterogeneities of the trabecular structure (100,101). This heterogeneity causes highly site-specific and direction-dependent material properties (102–107). Thus, the anisotropy of trabecular bone is location-dependent (108). Its structure as a porous cellular solid means that trabecular bone could absorb large quantities of energy before failure due to the fracture of individual trabeculae (74,109). Although the modulus of trabecular bone is significantly lower than that of cortical bone, the cellular structure of trabecular bone could possibly act synergistically with the surrounding cortical bone in order to enhance the material properties of the whole bone (110).

Similar to cortical bone, aging causes reductions in density, modulus, and strength (75,111,112). For trabecular bone, the number and thickness of the trabeculae are

decreased, and the size of the intertrabecular spaces increase (113–116). As transverse struts of the trabecular become thinner and fail, the anisotropy increases with age (112,117), and the longitudinal struts become more likely to buckle (118). In addition, the mechanical integrity of the collagen network also degrades with aging (90).

The modulus and strength of trabecular bone show a weak dependence on strain rate (119,120). An increase in the strain rate by 100-fold results in increases in both strength and modulus by 30% (108).

2.5 Bone Damage and Repair

The mechanical property degradation of bone loaded under repetitive loading is caused by damage, which initiates at the collagen and mineral level (121). As the cracks accumulate, they become visible using microscopy. Several experiments have demonstrated that repetitive loading *in vivo* causes microcracks to form in bone (122,123). The presence of microcracks have also been confirmed in several human bones, including the femur (124), tibia (124), and vertebrae (125,126). In these studies, microdamage in cadaveric bone was observed using microscopy. In order to differentiate the artefactual damage caused by preparation from the damage caused *in vivo*, bulk staining of larger segments of the bone was performed before preparing the thin sections required for histology (127). Several independent groups have used and verified this technique to show that *in vivo* microdamage exists in human bone (124–126).

Histological studies have also shown that the damage accumulates with age (128).

Typical microcracks that form during repetitive loading cycles are approximately 100 μm wide and 450 μm long (129). In order to repair damaged bone, osteoblasts and osteoclasts form teams called basic multicellular units (BMUs), which form cavities of approximately 200 μm long, and travel at a speed of approximately 40 μm per day (130). During the repair process, the BMUs are directed to the location of damage (122,123,131–135). The osteoclasts first break down the damaged bone, which are then followed closely by osteoblasts that deposit new bone and fill in the cavities. (130). Bone metabolism is regulated by hormones such as parathyroid hormone, calcitonin, calcitriol, growth hormone, thyroid hormone, estrogen, and testosterone. Other molecules involved in the regulation of bone metabolism include vitamin D, glucocorticoids, insulin-like growth factors, prostaglandins, and cytokines (73,136).

2.6 Stress Fracture Pathophysiology

Stress fractures are partial or complete fractures of the bone caused by the repetitive application of loads which are less than that required to fracture a bone in a single loading situation (55). There are two hypotheses relating the role of bone repair to the pathophysiology of stress fractures: the primary microdamage hypothesis, and the primary remodeling hypothesis (28). According to the primary microdamage hypothesis, the rate of microdamage accumulation exceeds the rate of bone repair. This could be caused by an abrupt change in duration, frequency, or intensity of training programs (14) or if the rate of bone formation is impaired (28).

On the other hand, the primary remodeling hypothesis states that stress fractures are caused by accelerated bone remodeling. This accelerated bone remodeling may be caused by genetics, increased stimuli for remodeling, systemic or reproductive hormones, or dietary intake (28,137). As bone resorption precedes formation during the repair response, the bone becomes temporarily weaker as bone is resorbed and resorption cavities are formed, making the bone more porous (138,139). As the replacement bone matrix is formed, it takes time for the new bone to fully mineralize, and the bone is in a weakened state. As a result, strains are higher in these weak areas and as a consequence more microdamage may form (140). Individual microcracks do not decrease the elastic modulus of bone (108), but the coalescence of microdamage creates larger cracks. The propagation of the larger cracks occurs slowly and causes a slight reduction of the elastic modulus (108). At this stage, the crack propagation is slowed by cement lines and other weakened interfaces. However, as larger cracks merge, crack propagation becomes faster as the weak interfaces fail to stop the cracks. Thus, the modulus decreases sharply and the bone fractures (108).

2.7 Metatarsal Stress Fractures

The metatarsal bones in the foot are a common site of stress fractures, accounting for approximately 9% of all stress fractures (1). The second metatarsal is the most common location for metatarsal stress fractures likely due to the high repetitive bending stresses experienced during running (1,2). In sports such as soccer, the fifth metatarsal is also a

common location for stress fractures (15) due to cyclic bending and torsional loads (141,142) associated with frequent changes in running speed and direction.

The occurrence of metatarsal stress fractures is especially high for elite soccer players, with up to 78% of all stress fractures presenting in the metatarsals (15). As metatarsal stress fractures cause an average of 14 weeks' absence due to injury (15), these prolonged injury durations can have a negative impact on a professional athlete's career (143) and on individual performance after recovery (144).

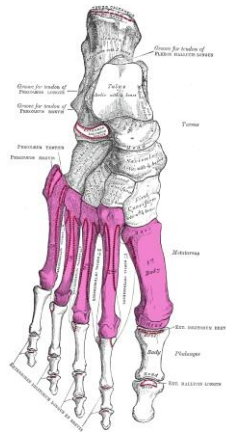


Figure 2-3. Transverse view of the bones in the right foot. Metatarsal bones are shown in purple. Image by Henry Vandyke Carter, 1858. Public domain. Retrieved from Wikimedia Commons: <https://commons.wikimedia.org/wiki/File:Gray268.png>

2.8 *In Vivo* Bone Strain Measurement

Several groups have attempted to measure bone strain *in vivo* using strain gauges in order to understand bone fatigue behaviour (145). The electrical resistance of the thin metal

comprising a strain gauge increases when stretched, and decreases when compressed. Thus, when a strain gauge consisting of one of these wires is firmly attached on a material, it can measure the strain in one direction. A single strain gauge could only measure the strain along its axis. However, three independent strain measurements are required at a given location in order to find all components of the strain tensor. The strain tensor could then be used to calculate the principal direction and principal strains (146). This method is typically implemented by using a strain gauge rosette, which is a set of three strain gauges oriented at different angles. Strain gauge rosettes have been attached directly to the bone, or fastened to bone staples, which were subsequently implanted in the bone.

2.8.1 Direct Strain Gauge Attachment

The first *in vivo* bone strain measurements on humans were performed by attaching strain gauges directly onto the surface of the bone (146). Typically, the first step of implanting rosette strain gauges onto the surface of human bones *in vivo* was the local anaesthetization of the tissue overlying the above the bone at which the strain gauge is to be inserted. This was usually followed by: 1) a 5-10 cm long incision through to the periosteum, 2) the removal of the periosteum, and 3) the cleaning of the bone surface. The strain gauges were then glued on to the bone surface with adhesive, and the wires of the strain gauges were passed through the opening of the wound and sutured to the periosteum. This strain gauge implantation procedure typically lasted approximately 1 hour, but the strain gauge was typically attached for up to 3 days for data collection

(147,148). In order to improve strain gauge bonding to the bone, the bone surface was sometimes degreased with alcohol or scored with a bone punch (148,149).

This method of strain gauge attachment had several disadvantages. The first was the quality of strain gauge attachment to the bone surface. It was difficult to evaluate *in vivo* bonding stability, and in some cases, strain gauges were not firmly attached and the data from the strain gauges were excluded from analysis (148).

2.8.2 Bone Staples with Strain Gauges

In order to reduce the invasiveness of the strain gauge implantation and to address the difficulties of strain gauge attachment to the bone surface, bone staples were used as a mounting device for the strain gauges (150,151). Before the bone staples were inserted, local anesthesia was applied and holes were drilled into the bone locations where the staples are to be anchored (151). Mounting rosette strain gauges requires three bone staples, with one staple per strain gauge (151). Although the use of bone staples required less invasive surgery and leaves the periosteum intact, strain gauges often failed or were damaged due to the surgery (152).



Figure 2-4. Medial X-ray view of instrumented staple inserted in the second metatarsal (7). Used with permission.

2.8.3 *In vivo Metatarsal Strain Results*

Strain gauges attached via bone staples were used to measure *in vivo* strains on the dorsal mid-diaphysis of the second metatarsal during barefoot (7) and shod (5) walking. For barefoot walking, maximum and minimum principal strains of $363 \pm 359 \mu\epsilon$ and $-1534 \pm 636 \mu\epsilon$ were measured, respectively (7). Maximum and minimum principal strains for shod walking were $761 \pm 383 \mu\epsilon$ and $-1144 \pm 297 \mu\epsilon$, respectively (5).

2.8.4 *Limitations of in vivo Measurement*

Apart from the disadvantages mentioned previously, one of the major shortcomings of *in vivo* strain gauge measurements is that the procedure for strain gauge implantation is very invasive. Swelling and tenderness at the site of incision was reported in most *in vivo* studies, and test subjects took several weeks to recover from the procedure (146).

Furthermore, *in vivo* strain measurements from the second metatarsal mid-diaphysis did not represent the strain in other sites of the second metatarsal (146). The strain distribution of the whole bone is important for understanding fatigue behavior because the fatigue life of bone has been hypothesized to be related to the stressed volume of the bone (153,154). Studies by Taylor on human and bovine bone samples of different sizes (153,154) have indicated that larger stressed volumes correspond with lower fatigue life due to a higher probability of finding weak regions. This concept of stressed volume has yet to be verified at the whole bone level. Therefore, having strain information for the whole bone could help quantify the stressed volume of bone, which may in turn elucidate the mechanisms underlying fatigue fractures.

2.9 The Finite Element Method

The finite element (FE) method is a numerical technique for approximating solutions to complex mechanical problems. FE models break down complex geometries into smaller units called elements, which are connected to each other at nodes. Each element is assigned material properties, which define how stiff the element behaves. The displacements are calculated at each node for a given loading scenario, using a set of equations that govern the force and moment equilibria of the nodes. From the displacements, the stress and strain distributions are calculated throughout the entire geometry of a body (155). Since strain is a quantity that is experimentally measured using strain gauges, experimental strain measurements can be used to validate FE predictions.

The computational cost of solving a finite element model depends on the number and type of elements in the model, as well as the material properties of the model. A higher number of elements results in a longer computational time to solve the models, as does the use of elements with a higher number of nodes. Non-linear material properties also increase the computational time for solving FE models.

The solution of FE models becomes closer to the exact solution as the number of elements increases, but is limited by image resolutions and the continuum assumption. That is, the solutions will not be accurate if elements become smaller than the size of the void spaces within the bone (156). As the continuing increase of computing power means that computational time is no longer a limiting factor in developing accurate FE models, it is important to perform convergence tests to ensure that the mesh density is sufficient to accurately capture the mechanical behaviour of bone (157).

Apart from the mesh refinement, the accuracy of finite element models also depends on the accuracy of the models' geometry and material properties. Over the years, the geometry of bones has improved from using generic and idealized two-dimensional models (158–160) to three-dimensional subject-specific models, which are becoming more commonly used (161). Bone geometries for the latter are typically generated using x-ray computed tomography (CT) or magnetic resonance imaging (MRI) scans (162,163).

As CT attenuations only provide a scalar value at each point, many studies assume isotropic elasticity (164–169), although anisotropic material properties have also been

implemented using information within the voxel (170). The elastic moduli for early isotropic models have been homogeneous (171–173), but more recent studies have used inhomogeneous materials (8,164,165,170,174–178) as they have been found to be more accurate than the models using homogeneous material properties (9,179,180). For inhomogeneous material properties, the elastic modulus is typically estimated using empirical equations that relate the bone density to modulus. Such empirical density-elasticity relationships have been identified for the human femur (102,181–185), tibia (102,117,186–188), pelvis (189), and vertebrae (102,183,190–192). The empirical equations have been found to be site-specific (102), and equations for cortical bone are different from equations for trabecular bone within the same gross anatomical location (193).

Density-elasticity relationships have also been developed using optimization techniques for the human femur (8,194,195), tibia (8,196), humerus (8), radius (8), and ulna (197). Such equations have shown that a single equation can be used for both the trabecular and cortical bone (194,195,197). However, the optimized density-elasticity equations still illustrate site- and cohort-specificity (194).

2.9.1 Verification and Validation of Finite Element Models

As with any type of model, finite element models must be verified and validated. Verification refers to the process of determining that a computational model represents the underlying mathematical model and its solution. Validation is the process of

determining the degree to which a model is an accurate representation of the real world from the perspective of the intended uses of the model (198).

One aspect of FE model verification and validation is the correct geometrical representation of the object to be modeled. The geometry of a bone can be obtained by reconstructing two-dimensional (199) or three-dimensional (200) bone images.

Therefore, the resolution of the images must be sufficient to capture the geometry of the bone at an appropriate level of detail.

Another aspect of verification is the construction of the finite element mesh. The mesh incorporates the elements and the nodes, so not only must the mesh capture the geometry of the bone, but the mesh resolution must also be high enough to accurately calculate the stresses and strains at each point (201). Since a finite element model with a high number of elements requires higher computational costs to solve, the finite element mesh should not exceed the necessary mesh density for convergence. The level of accuracy required for the FE model depends on the model's intended use (202) and output parameter. For inhomogeneous FE models of bones, a convergence criteria of within 5% of the converged solution is typically used (177).

To validate the finite element models, the results of the model calculations are compared with either analytical calculations or experimental measurements. Since analytical solutions to problems involving the complex geometries and inhomogeneous material

properties of bones are very complicated if not impossible, experimental measurements are often used to validate finite element models of bones.

2.10 Summary of Literature Review

This literature review has examined the current research related to stress fractures, the mechanics of bone, *in vivo* strain measurement in bone, and finite element modeling. A knowledge gap currently exists regarding finite element modeling of the human metatarsal. The study outlined in Chapter 3 presents a finite element model of the human metatarsal, which was validated using experimentally-measured strains.

**Chapter Three: EXPERIMENTAL VALIDATION OF FINITE ELEMENT
PREDICTED BONE STRAIN IN THE HUMAN METATARSAL**

Submitted to: Journal of Biomechanics

Authors: Anita Fung^{1,2,3}, Lindsay Loundagin^{1,3}, W. Brent Edwards^{1,2,3}

¹ Human Performance Laboratory, Faculty of Kinesiology, University of Calgary

² Biomedical Engineering Graduate Program, University of Calgary

³ McCaig Institute for Bone and Joint Health, University of Calgary

3.1 Abstract

Metatarsal stress fracture is a common injury observed in athletes and military personnel. Mechanical fatigue is believed to play an important role in the etiology of stress fracture, which is highly dependent on the resulting bone strain from the applied load. The purpose of this study was to validate a subject-specific finite element (FE) modeling routine for bone strain prediction in the human metatarsal. Strain gauge measurements were performed on 33 metatarsals from seven human cadaveric feet subject to cantilever bending, and subject-specific FE models were generated from computed tomography images. Material properties for the FE models were assigned using a published density-elasticity relationship as well as density-elasticity relationships developed from optimization techniques. The optimized relationships were developed with a ‘training set’ of metatarsals (n=17) and cross-validated with a ‘test set’ (n=16). The published and optimized density elasticity equations provided FE-predicted strains that were highly correlated with experimental measurements for both the training ($r^2 \geq 0.95$) and test ($r^2 \geq 0.94$) sets; however, the optimized equations reduced the maximum error by 10% to 20% relative to the published equation, and resulted in an X=Y type of relationship between experimental measurements and FE predictions. Using a separate optimized density-elasticity equation for trabecular and cortical bone did not improve strain predictions when compared to a single equation that spanned the entire bone density range. We believe that the FE models with optimized material property assignment have a level of accuracy necessary to investigate potential interventions to minimize metatarsal strain in an effort to prevent the occurrence of stress fracture.

3.2 Introduction

Stress fractures are common injuries in athletic and military populations. This type of fracture makes up 10% of athletic injuries (1), and up to 5% of injuries experienced by military recruits (11). In the US Marine Corps, stress fractures are the single most costly injury (\$5 million per year) due to lost training time, medical and rehabilitation expenses, and trainee attrition (203). Some 10%-20% of all stress fractures occur in the metatarsals bones of the foot (3), presumably because of their long narrow diaphyses and the large bending loads they experience during gait (204).

Mechanical fatigue is a well-accepted proposed mechanism in the pathophysiology of stress fracture (4,121,205). Mechanical fatigue is defined as the progressive loss of material stiffness and strength due to repetitive loading. This process is highly dependent on the resulting strain from the applied mechanical load (4). Several studies have measured metatarsal strains *in vivo* during locomotion using strain gauges applied directly to the periosteal surface (5–7). However, *in vivo* strain gauge measurement is highly invasive and limited to small, localized regions of the bone surface. As a consequence, computational modeling approaches such as the finite element (FE) method have become increasingly important for strain estimation (8,9).

FE models can be generated on a subject-specific basis using geometry and material property information obtained directly from computed tomography (CT) images. Models with inhomogeneous material properties are more accurate than those with homogeneous

material properties (9,179,180), and in the former case, material properties are typically assigned using functions based on relationships between bone apparent density and elastic modulus. Although many density-elasticity relationships have been experimentally determined for bones such as the femur (181–183), tibia (117,186,187), pelvis (189), and vertebrae (183,190), no empirical equations have been developed for human metatarsals. This may be due, in part, to difficulties in extracting small samples of bone from the metatarsals for apparent-level material testing. It is important to verify if a density-elasticity equation from another anatomical location would be appropriate for metatarsal strain estimation.

As an alternative to experimental testing, density-elasticity equations for the human femur (8,194,195), tibia (8,196), humerus (8), radius (8), and ulna (197) have been developed using optimization techniques. These studies typically assume an equation of the form $E=a\rho^b$, where E is the elastic modulus, ρ is the density, and a and b are unknown coefficients determined by minimizing the error between experimental measurements and FE predictions. The majority of these studies have illustrated that a single optimized density-elasticity equation spanning the entire density range provides sufficiently accurate FE predictions (194,195,197).

The purpose of this study was to verify and validate a subject-specific FE modeling routine for strain estimation in the human metatarsal. To this end, a combined numerical-experimental study was performed in which strain gauge measurements from mechanical tests were directly compared with strain predictions from FE models. A published

density-elasticity equation was examined and directly compared to density-elasticity equations calculated using optimization techniques. It was hypothesized that FE models using optimized density-elasticity relationships would provide more accurate metatarsal strain predictions than FE models using the published relationship.

3.3 Methods

3.3.1 Specimens

Seven fresh-frozen human cadaveric feet were obtained from the Body Donation Program at the University of Calgary following institutional ethics approval. The specimens were acquired from four separate donors (2 male, 2 female) ranging in age from 73 to 95 years. Detailed demographic information of each donor is listed in Table 3-1.

Table 3-1. Cadaver demographic information.

Cadaver ID	1	2	3	4
Age (years)	85	73	78	95
Feet obtained	Left and Right	Right	Left and Right	Left and Right
Height (cm)	180	178	157	163
Weight (kg)	70	72	73	45
Gender	Male	Male	Female	Female
Cause of Death	Pulmonary Embolism	Alzheimer's	Bilateral Pneumonia, Severe COPD	Dementia

3.3.2 Imaging Acquisition

Cadaveric feet were thawed overnight to room temperature and CT images were obtained using a Revolution CT (General Electric Healthcare; WI, USA) at the University of

Calgary's Centre for Mobility and Joint Health. The feet were placed on a custom-made wooden jig during scan acquisition to align and maintain the limb in a static, neutral position. A calibration phantom containing three known calcium hydroxyapatite solution inserts of 100, 400, and 800 mg/cm³ (QRM GmbH; Möhrendorf, Germany) was included in each scan. The CT scan acquisition parameters were as follows: tube current 220 mA, peak voltage 120 kVp, pitch=1, in-plane resolution 0.39 mm, and between-plane resolution 0.625 mm (206).

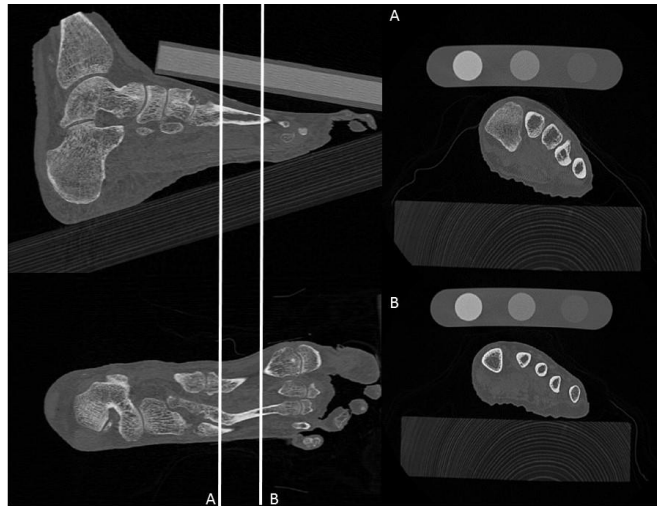


Figure 3-1. Sagittal (top left) and transverse (bottom left) views of a representative CT scan. Lines A and B depict the location of the proximal (top right, A) and distal (bottom right, B) frontal views of the metatarsals. The calibration phantom is visible in the sagittal and frontal views along with the wooden jig used to align the foot during scanning.

3.3.3 Mechanical Testing

Metatarsals were excised and the proximal-most 2 cm of each bone were potted in an aluminum cylinder using bone cement (Fastray, Harry J. Bosworth Company, Skokie, IL). Select anatomical landmarks were subsequently digitized using a FARO Arm (FARO Technologies Inc., FL, USA) including: three points on the distal potting surface, one point at the centre of the proximal potting surface, the most distal point of each metatarsal, the plantar-most points of each epicondyle, and a marked location where strain gauges were to be adhered (i.e., dorsal mid-diaphysis). Rectangular strain gauge rosettes (UFRA-1-350-11-1L, Tokyo Sokki Kenkyujo Co., Ltd., Tokyo, Japan) were adhered with cyanoacrylic glue at the marked locations of the dorsal surface of each metatarsal after the surface was sanded and cleaned with isopropyl alcohol. The longitudinal direction of each rosette (i.e., the 2nd strain gauge element) was oriented parallel to the long axis of the metatarsal.

A custom fabricated aluminum fixture was used to position the metatarsals at 38°, 33°, 30°, 28°, and 24° for the first through fifth metatarsals, respectively (Figure 3-2). These angles corresponded to the instant of peak metatarsal stress during the stance phase of running (204). Vertical ramped displacements were applied to the plantar surface of the metatarsal heads at a constant rate of 1 mm/s using an MTS materials testing machine (MiniBionix 858, MTS Systems, MN, USA). The magnitude of applied displacement varied between 1-3 mm, depending on metatarsal, in an effort to keep strains in the linear-elastic range. Displacements were applied through a bolt (9.4 mm in diameter)

with a thin layer of silicone for load distribution. Three replicate trials were performed for each bone. Displacement, force, and strain measurements were collected synchronously at a sampling frequency of 500 Hz using a high-precision data acquisition system (System 8000, Vishay Precision Group – Micro-Measurements; Raleigh, NC, USA).

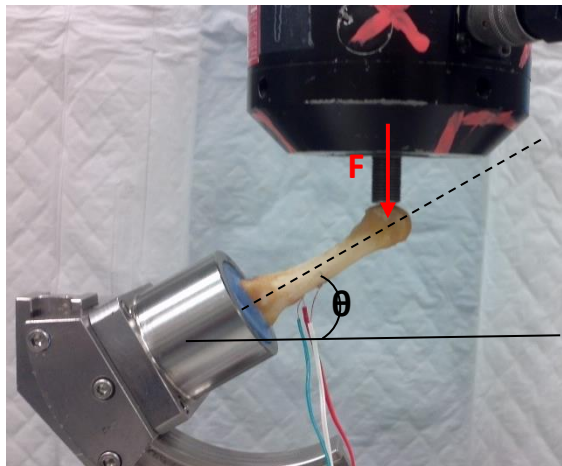


Figure 3-2. Photo of a representative experimental test set-up. A displacement/force was applied to the plantar surface of the metatarsal (denoted by arrow F) while the metatarsal was positioned at angle θ in the aluminum pot. Periosteal strain gauges are visible on the dorsal surface of the diaphysis.

3.3.4 Finite Element Modeling

Metatarsals from the CT scans were segmented and meshed with quadratic tetrahedral elements using the Mimics Innovation Suite (Materialise, Leuven, Belgium). The maximum element edge length was set to 3 mm corresponding to median element edge lengths between 1.0 and 1.5 mm, depending on metatarsal. This level of refinement was

chosen in accordance with a preliminary mesh convergence analysis examining maximum element edge lengths ranging from 2 to 8 mm (increments of 1 mm), corresponding with median element edge lengths from 0.2 to 5.7 mm. Decreasing the maximum element edge length from 4 to 3 mm changed principal stresses, principal strains, and maximum displacements by less than 5%. The number of nodes for each FE model at the selected mesh density ranged from 15,858 to 38,879, while the number of elements ranged from 10,291 to 26,689, depending on metatarsal.

FE models were assigned inhomogeneous isotropic linear-elastic material properties based on bone apparent density using a combination of Mimics and MATLAB software (Mathworks, Natic, MA). The Hounsfield units for CT voxels comprising each segmented bone were converted to units of apparent density using a linear calibration equation developed with the phantom. Elements were assigned an apparent density value based on the average of all voxels contained within the element. To mitigate partial volume effects, apparent density assignment was constrained to a segmented mask eroded by 1 voxel from the bone periosteal surface. In the event that an element fell outside of this mask, it was assigned the density value of their nearest neighbouring element. An elastic modulus was subsequently assigned to each element based on 1) a previously published density-elasticity relationship (Figure 3-3a), or 2) density-elasticity relationships obtained through optimization (see *Density-Elasticity Equations and Optimization*). The Poisson's ratio for all elements was set to 0.3 in accordance with previous FE models of human bone (8,164,207,208).

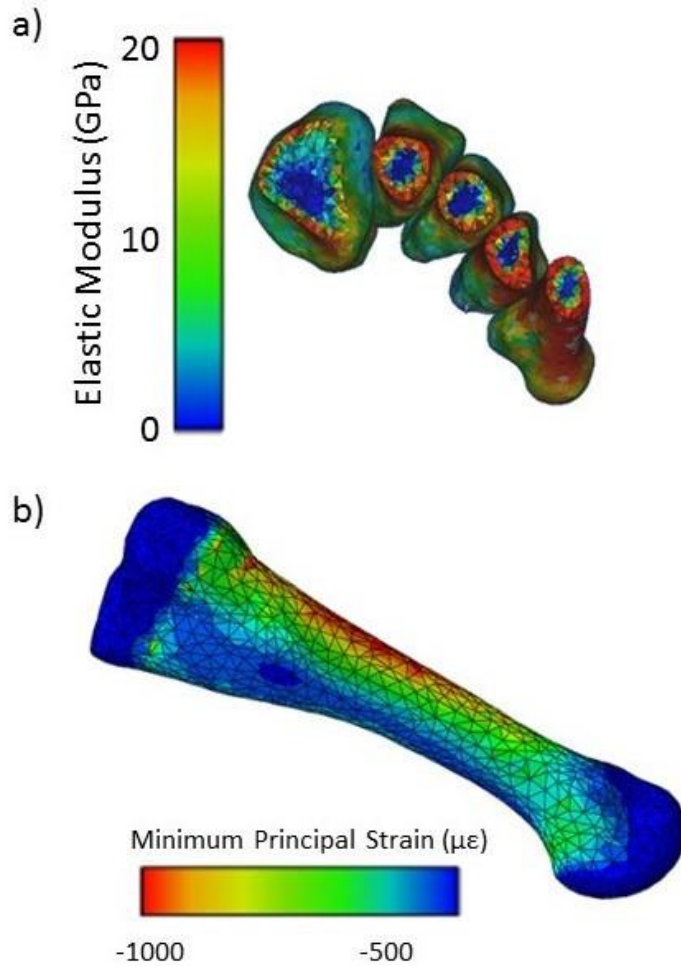


Figure 3-3. a) Representative cross-sectional view of the elastic modulus distribution for the published density-elasticity equation (187) and b) FE-predicted minimum principal strain distribution for a second metatarsal loaded in cantilever bending.

The boundary conditions of the FE models replicated the mechanical tests. The locations of potting, load application, and strain gauge locations in the FE model coordinate system were identified using transformation equations based on digitization data from the FARO Arm. The FE models were rotated in a global reference frame such that their angles were identical to mechanical testing. Surface nodes at the location of proximal potting were

fully constrained in three dimensions and a ramped vertical load was applied to the plantar surface of the metatarsal head. The point of load application was coupled with surface nodes within a 4.7 mm radius to match the dimensions of the bolt used to apply load during mechanical testing. All FE models were solved using ABAQUS Standard v6.1 (ABAQUS Inc., RI, USA). The computation of a single FE model took approximately 10 to 20 seconds on a typical 6-core workstation; however, the process of generating the input files and reading the output files in MATLAB took more than 10 minutes per model.

3.3.5 Density-Elasticity Equations and Optimization

The previously published density-elasticity relationship was specific to proximal tibia bone (187): $E = 0.51\rho_{app}^{1.37}$, where E is the elastic modulus in MPa, and ρ_{app} is the apparent density in kg/m^3 . This particular density-elasticity equation was chosen over other empirical relationships (e.g., those from (102) and (209)), because a preliminary sensitivity analysis suggested it provided FE strain predictions on the order of those directly-measured *in vivo* during barefoot (7) and shod (5) walking. A single and a piecewise density-elasticity equation were developed using Nelder-Mead minimization of the root-mean-squared-error (RMSE) between measured and FE-predicted maximum and minimum principal strains (210) at the digitized strain gauge locations. The single equation spanned the entire density range, while the piecewise equation had a separate density-elasticity relationship for trabecular and cortical bone. Equations took the form of $E = a\rho_{app}^b$, where a and b are unknown constants solved with optimization.

The Nelder-Mead optimization method was used to develop the optimized density-elasticity equations. This method constructs a simplex based on initial guesses of the function to be minimized. A simplex is a geometrical shape which has $n+1$ vertices in n dimensions. For the Nelder-Mead optimization algorithm, n is the number of unknown variables. At each iteration of the optimization, the algorithm compares the function values at the different vertices of the simplex and replaces the worst vertex, which is the point with the highest function value, with a new point with a lower function value. This new point is calculated by reflecting the simplex about the edge that is opposite the worst point, and either expanding, contracting, or shrinking the simplex until a point with a lower function value is identified (211). This process continues as the values at the simplex vertices get successively smaller, and eventually converges to a minimum.

The optimized single density-elasticity equation took the form $E=a\rho_{app}^b$, where E is the elastic modulus, ρ_{app} is the apparent density of the element, and a and b are unknown constants to be determined. Since the variable a can vary between several orders of magnitude depending on the exponent b , and is thus difficult to estimate, a was instead calculated indirectly by solving for the modulus at a known density. The density was set to the average apparent density of cortical bone (i.e., 1.86 g/cm^3) (117), and the unknown modulus, $E_{1.86}$, was set as the second variable to be determined. Therefore, the unknown variables in the optimized single density-elasticity equation were actually $E_{1.86}$ and b . Three initial estimates were needed to construct the vertices of the simplex for the Nelder-Mead optimization algorithm for the single equation. For the initial estimates,

random values for exponent b were restricted between 1 and 4, in accordance with values found in the literature (212). $E_{1.86}$, the elastic modulus at an apparent density of 1.86 g/cm³, was restricted to values between 10 and 20 GPa, which is consistent with the material properties of cortical bone (117,213,214).

The optimized piecewise density-elasticity equation took the form $E_{trab}=a_1\rho_{app}^{b_1}$ and $E_{cort}=a_2\rho_{app}^{b_2}$, where E_{trab} is the elastic modulus of trabecular bone, E_{cort} is the elastic modulus of cortical bone, ρ_{app} is the apparent density of the element, and a_1 , b_1 , a_2 , and b_2 are constants to be determined. A threshold density, ρ_{thres} , that distinguished between trabecular and cortical bone elements was also included as an unknown parameter in the optimization. Initial estimates of parameters b_1 and b_2 were restricted to values between 1 and 4 (212) and ρ_{thres} was constrained to a range of 0.5 to 1.0 g/cm³, following the maximum trabecular bone densities in previous studies (102,181,191). For cortical bone equations, parameter a_2 was indirectly calculated by setting the modulus to a value of $E_{1.86}$ between 10 and 20 GPa (117,213–215). Since a_2 is dependent on $E_{1.86}$, the optimization contained five independent unknown parameters: a_1 , b_1 , b_2 , $E_{1.86}$, and ρ_{thres} . Six different combinations of the unknown parameters were randomly generated and served as initial guesses for the piecewise density-elasticity equations. Each of the six sets of density-elasticity equations were assigned to the 17 finite element models in the training set.

The root-mean-square error (RMSE) was calculated at each of the different combinations of unknown parameters in the single and piecewise optimization routines:

$$f(\mathbf{x}) = \sqrt{\frac{\sum_{t=1}^n (\hat{\varepsilon}_t - \varepsilon_t)^2}{n}}$$

where the measured principal strains are represented by the variable $\hat{\varepsilon}$, and the FE-predicted principal strains are denoted by ε . The variable n represents the total number of strain values, which included both maximum and minimum principal strains. For the single equation, $\mathbf{x}=(E_{1.86},b)$, while for the piecewise equation, $\mathbf{x}=(a_1, b_1, b_2, E_{1.86}, \rho_{thres})$. Once the RMSE and the initial simplex were obtained for each combination of initial guesses, the Nelder-Mead algorithm was implemented to find the minimum RMSE between the measured and FE-predicted strains. The algorithm was implemented using a custom MATLAB program, which executed Python scripts which interacted with the FE solver, ABAQUS. For each iteration and each modification to the simplex, all of the FE models in the training set were solved with the parameter combination at the new vertex of the simplex. For the piecewise equation, an additional constraint was added to the algorithm so that the maximum density of trabecular bone did not exceed the minimum density of cortical bone. To verify if the resulting parameters corresponded to a global RMSE minimum, a new set of initial guesses were generated, and the optimization algorithm was run again until the same minimum was obtained. The time taken to run the entire optimization algorithm was approximately 18 hours on a typical 6-core workstation.

In order to verify the robustness of the equations obtained through optimization, the metatarsals were split into a ‘training set’ and ‘test set’. The training set was used to develop the custom density-elasticity equations using the optimization algorithm, while the test set was used for cross-validation. Note that the training and test sets for the published density-elasticity equation were only used for a direct comparison to the optimized equations. The metatarsals were assigned to either set based on volumetric bone mineral density (vBMD). The entire sample was ranked according to vBMD, and alternate rankings were assigned to each set. Seventeen metatarsals were allocated to the training set, and sixteen metatarsals were allocated to the test set. The remaining two metatarsals were broken during testing and were not included in the analysis.

3.3.6 Data Reduction and Statistical Analysis

The maximum and minimum principal strains from experimental strain gauge rosette measurements were calculated and the three replicate trials were examined to ensure repeatability and linear-elasticity. The three-dimensional FE-predicted strains at the strain gauge location of each metatarsal were transformed into a local planar coordinate system with a unit normal to the bone periosteal surface. Elements within a 4.0 mm radius of the digitized point were included in this calculation to be consistent with the size of the strain gauge rosette. The maximum and minimum FE-predicted principal strains at this location were statistically compared to the mean principal strains from the three repeated experimental measurements at a common load of 25 N. Statistical metrics, including Pearson's r correlation, linear regression, RMSE, and maximum error, were calculated

separately for the training and test sets. Statistical analysis was performed using SPSS v24 (IBM Corp, Armonk, NY) with the criterion alpha level set to 0.05.

3.4 Results

3.4.1 Experimental Strain Measurements

Experimental strain measurements demonstrated high inter-trial repeatability, with a difference in measurements between replicate trials of less than 5%. Residual strains were low, at less than 5% of the peak value immediately after load removal, thus confirming linear-elastic mechanical behaviour. The mean principal strains at 25 N from the three replicate trials ranged from $-1231 \mu\epsilon$ (i.e., compression) to $631 \mu\epsilon$ (i.e., tension), depending on metatarsal.

3.4.2 Published Density-Elasticity Equation

The published density-elasticity equation provided FE-predicted strains (Figure 3-3b) that were highly correlated with experimental measurements for both the training ($r^2=0.95$) and test ($r^2=0.94$) set (Table 3-2). The regression line for the training set illustrated a slope significantly less than 1 and an intercept not different than 0, indicating that the model tended to overestimate experimental strains (Figure 3-4a). On the other hand, the regression line for the test set illustrated a slope that was not significantly different from 1, and an intercept that was not significantly different from 0 (Figure 3-4b), indicating an

X=Y type of relationship. The maximum error for the training and test sets were 37% and 44% of the highest measured strain, respectively.

Table 3-2. Validation parameters for the training and test sets as a function of published and optimized density-elasticity equations.

	$E = 0.51\rho_{app}^{1.37}$		$E = 2.39\rho_{app}^{1.15}$		$E_{trab} = 6.01\rho_{app}$ $E_{cort} = 1.06\rho_{app}^{1.26}$ $\rho_{thres} = 719 \text{ kg/m}^3$	
	Training Set	Test Set	Training Set	Test Set	Training Set	Test Set
Slope	0.92 ^a	0.95	1.03	0.99	1.01	0.96
Intercept	12.75	3.05	16.94	5.46	14.97	4.82
R	0.98	0.97	0.98	0.98	0.98	0.98
R²	0.95	0.94	0.96	0.95	0.96	0.95
RMSE ($\mu\epsilon$)	101.03	81.61	81.93	74.70	80.73	75.12
RMSE (%)^b	8.21	10.18	6.66	9.32	6.56	9.37
Max Error ($\mu\epsilon$)	456.32	348.38	211.34	216.76	231.87	272.03
Max Error (%)^b	37.07	43.47	17.17	27.05	18.84	33.94

^a Significantly different from 1 (slope).

^b Percentage of the maximum absolute measured strain.

3.4.3 Optimized Single Density-Elasticity Equation

The optimized single density-elasticity equation for the training set was $E = 2.39\rho_{app}^{1.15}$, where E is the elastic modulus in MPa, and ρ_{app} is the apparent density in kg/m^3 . This equation provided an r^2 of 0.96 for the training set and 0.95 for the test set (Table 3-2).

Both the training (Figure 3-4c) and test (Figure 3-4d) sets illustrated regression slopes not different than 1 and intercepts not different than 0. The optimized single density-elasticity equation provided an improvement to the maximum error when compared to the published density-elasticity equation (Table 3-2).

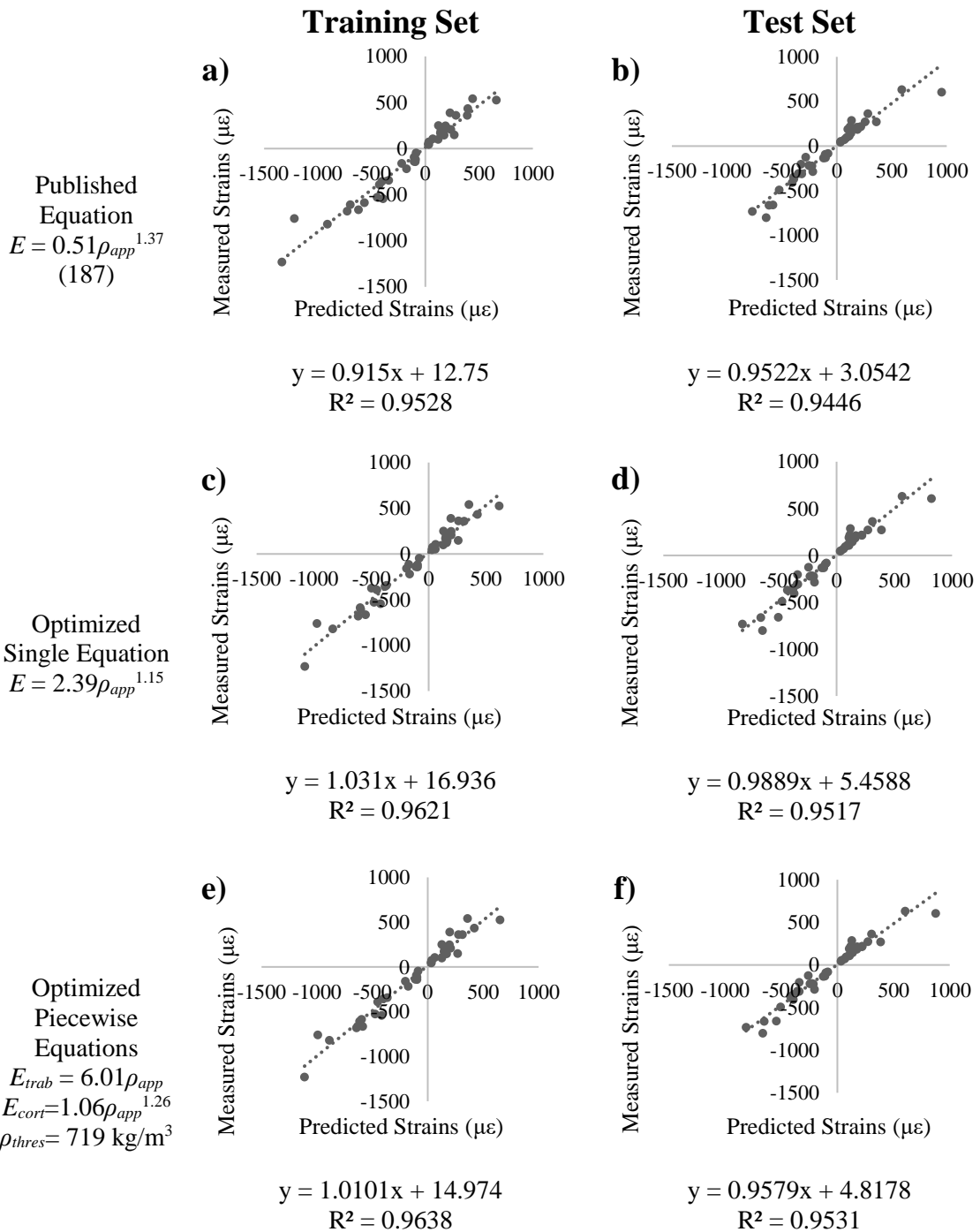


Figure 3-4. Measured vs. predicted principal strains at 25 N for metatarsals using the published equation: a) training set, and b) test set; optimized single equation: c) training set, and d) test set; and optimized piecewise equations: e) training set, and f) test set.

3.4.4 Optimized Piecewise Density-Elasticity Equation

The optimized piecewise density-elasticity equation for the training set with separate equations for trabecular and cortical bone was $E_{trab} = 6.01\rho_{app}$ and $E_{cort} = 1.06\rho_{app}^{1.26}$. The threshold density separating trabecular from cortical bone was $\rho_{thres} = 719 \text{ kg/m}^3$. Similar to the optimized single equation, the optimized piecewise equation provided an X=Y type of relationship for both the training (Figure 3-4e) and test (Figure 3-4f) set, with the r^2 being 0.96 and 0.95 for the training set and test set, respectively. The optimized piecewise density-elasticity equation also provided an improvement to the maximum error when compared to the published density-elasticity equation (Table 3-2).

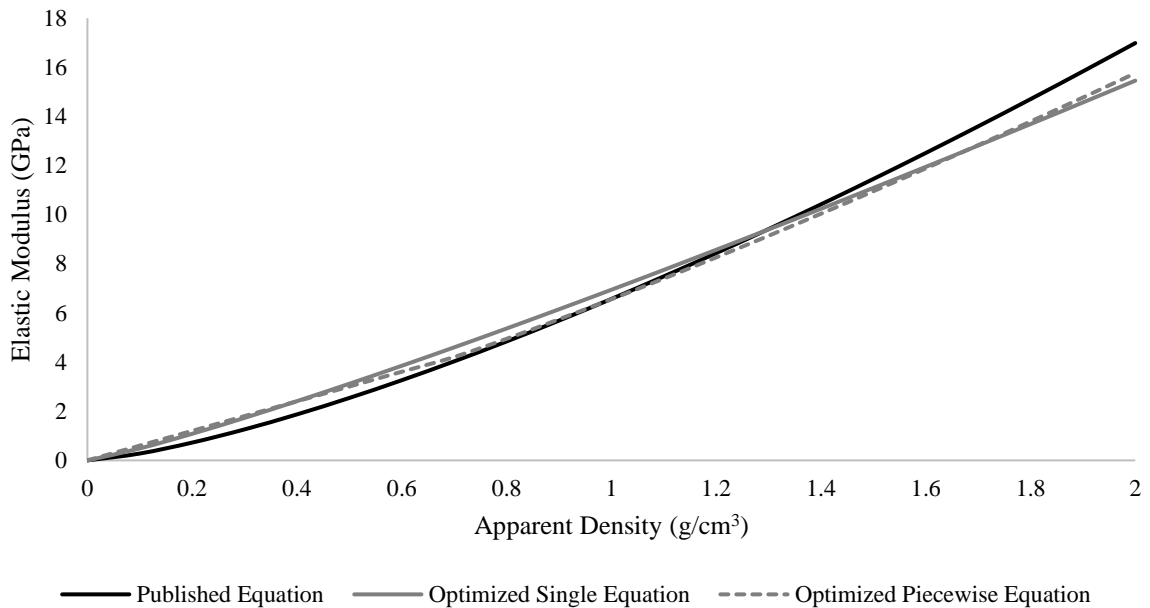


Figure 3-5. Elastic modulus vs. apparent density for the published and optimized density-elasticity equations.

3.5 Discussion

Bone strain plays an important role in the mechanical fatigue of bone (4), which may contribute to the pathophysiology of stress fracture (17). A considerable number of these fractures occur in the metatarsals, and the purpose of this study was to verify and validate a subject-specific FE modeling routine for the non-invasive prediction of metatarsal bone strain. The accuracy of a published density-elasticity relationship as well as an optimized single and piecewise density-elasticity relationship were examined. Both the single and piecewise equations reduced the maximum error of the models relative to the published equation, and resulted in an X=Y type of relationship between experimental measurements and FE predictions.

The published density-elasticity equation provided metatarsal strain predictions that were highly correlated with experimental measurements ($r^2 \geq 0.94$), in accordance with some of the better FE predictions reported in the literature for other bones (209,216,217).

Although the test set illustrated an X=Y type of relationship, the training set illustrated a regression slope that was significantly less than unity, indicating an over-prediction of bone strain with the published density-elasticity relationship. It is interesting, but not entirely surprising, that an empirically derived density-elasticity equation specific to the proximal tibia provided such an accurate prediction of metatarsal bone strain using the FE method. The tibia and metatarsals are both long bones of the lower-extremity that illustrate a comparable trabecular-cortical bone ratio relative to other skeletal regions, and

experience a similar mechanical loading environment during locomotion (5) with relatively high bending loads.

The optimized density-elasticity equations provided strain predictions that were just as correlated, but lower in maximum error, when compared to predictions with the published equation. Both Cong et al. (195) and Eberle et al. (194) used optimization techniques to develop density-elasticity equations for FE models of the human femur. These studies calculated a single power law equation that spanned the entire density range with an exponent of 1.16, which is nearly identical to that obtained for the optimized single equation in the present study (i.e., 1.15). These exponents are lower than those previously obtained in empirical studies (119,179,187), which were higher than 1.3. Eberle et al. (194) suggested that although the influence of fabric is typically captured in power laws for trabecular bone density-elasticity relationships (218,219), cortical bone has a more linear density-elasticity relationship (187,218) and tends to dominate the behaviour of whole bone. In the present study, all of the optimized equations were able to generate an $X=Y$ relationship with an RMSE under 10%. The results indicated that a single density-elasticity equation is adequate for the entire density range when using the FE method to predict human metatarsal strains.

Unlike previous empirical studies (181,186,220), the optimized trabecular bone density-elasticity equation from the piecewise relationship of the present study was linear ($E_{trab} = 6.01\rho_{app}$). Metatarsals in this study were subjected to cantilever bending, in which the highest stresses would be expected to occur at the cortical bone surface. In this respect,

the trabecular bone and fabric would have little influence on the mechanical behaviour of the metatarsal. The apparent density threshold obtained for the optimized piecewise equation was 0.77 g/cm^3 . This is slightly lower than the threshold density of 1 g/cm^3 reported in other studies (178,221). The lower density threshold may be attributed to the age of our donors, which is known to reduce the density of both cortical and trabecular bone (75). Just as it is possible that a density-elasticity relationship is specific to a given cohort (194), it is likely that a density threshold is cohort-specific as well.

Although a considerable number of bones were used in this study when compared to other validation experiments (209,216), it is important to note that these bones came from a small number of donors ($n=4$) of advanced age. Any potential differences in bone tissue quality of a younger cohort (90,222) may lead to a systemic overestimation of bone strain using the modeling approach and density-elasticity equations developed herein, because the CT-based FE models would not capture important details related to bone microarchitecture or the mechanical integrity of the collagen network (90,222).

Additionally, the relatively low resolution of clinical CT makes it difficult to structurally separate and independently mesh trabecular from cortical bone using traditional segmentation approaches. This limitation may be overcome by using algorithms similar to those suggested by Pakdel et al. (223), which estimates local dimensions of sub-mm bone features whose images are degraded by the limited resolution of clinical CT scanners. Another limitation of the current study is that metatarsals were loaded at a fixed angle, in a single mode of loading (i.e., bending), at a relatively low magnitude. It remains unclear how accurate FE strain predictions would be at different angles of

applied load, under more complex modes of loading, or at loading magnitudes beyond the linear-elastic range.

3.6 Conclusions

A published density-elasticity relationship specific to the proximal tibia provided FE-predictions that were highly correlated with experimental strains in the human metatarsals. The model overestimated strains in some instances, and utilization of an optimized density-elasticity equation provided an X=Y type of relationship and lower maximum error values by 10% to 20%. A piecewise relationship that modeled trabecular and cortical bone independently was no more accurate than a single density-elasticity equation spanning the entire density range. We believe that the FE models with optimized material property assignment have a level of accuracy necessary to investigate potential interventions to minimize metatarsal strain in an effort to prevent the occurrence of stress fracture.

3.7 Acknowledgements

The authors would like to thank Mehdi Shekarforoush, Majid Nazemi, the University of Calgary Centre for Mobility and Joint Health, and the University of Calgary Body Donation Program for their assistance with this project. This work was partly funded by the Natural Sciences and Engineering Research Council of Canada (WBE; RGPIN 01029-2015).

Chapter Four: CONCLUSION

4.1 Summary of Study

The objective of this thesis was to verify and validate a subject-specific finite element modeling routine for strain estimation in the human metatarsal. Results were obtained using a combined numerical-experimental study. It was hypothesized that finite element models using optimized density-elasticity relationships would provide more accurate metatarsal strain predictions than FE models using a published relationship. From the results, the regression equation between the experimentally-measured and the FE-predicted strains had a high correlation, but overestimated the strains in some instances. Custom density-elasticity equations were developed using optimization techniques, and provided an X=Y type of relationship between measured and predicted strains for both the training set and test set. The maximum error between measured and predicted strains for the custom equation were reduced by 10% to 20% when compared to the published equation. The use of separate density-elasticity equations for trabecular and cortical bone did not appear to further improve FE strain estimations when compared to the single custom equation.

Since there were no published density-elasticity relationships specific to the metatarsal, we selected an equation from another anatomical site for comparison. Although preliminary sensitivity tests using the equation resulted in strains similar to *in vivo* results in the literature (5,7), the validation study showed a systematic strain overestimation in

some bones, as shown in Figure 3-4a. These results underscore the importance of validating FE models and ensuring that the density-elasticity relationship is suitable for the models. The improvement of the FE strain predictions with the custom equations shows the feasibility of optimization techniques to develop density-elasticity equations if none of the published equations are suitable.

4.2 Study Limitations

Bone exhibits anisotropic behavior, but the FE model presented in this study assumed isotropic material properties. Although the FE predictions were validated with the isotropic model, it is unknown whether the isotropic model is valid for other loading conditions. Several previous studies of the femur incorporating anisotropy (224–226) have demonstrated minor changes to FE stress predictions compared to the isotropic model. However, two other studies (170,227) have found that the anisotropic material properties had a significant effect at certain locations on the model, depending on the model's boundary and loading conditions. A study on FE models of the human metacarpal (216) found that anisotropic material properties improved FE predictions for torsional and combined axial and bending loads. To our knowledge, anisotropic FE modeling of the metatarsals have not yet been implemented. However, if anisotropic material properties are to be implemented, there are several ways to obtain the required information for the model. One way is to perform mechanical tests on small bone samples in different orientations to obtain the appropriate engineering constants (228–230), although the mechanics tests are often subject to end effects (100). Ultrasonic

methods could also be used to evaluate elastic constants on small bone specimens, but this does not account for the tissue's heterogeneity (162) or post-yield mechanical behavior. Furthermore, it may be impractical to extract such small bone samples from relatively small bones such as the metatarsals. Investigators have also used voxel gradients within groups of voxels to quantify bone tissue anisotropy (170). For trabecular bone, the mean intercept length of the tissue could also quantify anisotropy. The mean intercept length (MIL) is the mean length of a line segment which passes through the specimen and is entirely contained within the specimen (231,232). The fabric tensor, which is a measure of local anisotropy, could be derived from the MIL measurements (233). This method to determine the anisotropic information could be implemented using micro-CT (234–236) or micro-MRI (237,238). The development of an anisotropic FE metatarsal model would also require validation. As the present study showed that isotropic models are sufficient to estimate metatarsal strains, additional loading conditions such as torsion and combined loads should be tested on both the isotropic and anisotropic FE models. The accuracy should be compared between the two models to determine whether anisotropy has an effect on strain estimations of FE metatarsal models.

The small number of cadaver donors ($n=4$) of advanced age (73-95 years) used for the specimens in this study also limits the applicability of the equations developed in this study. Depending on the application, model validation using specimens representing a larger cross-section of the population may be needed before these models are used to investigate potential interventions to prevent injury.

The linear-elastic assumptions for the material model also limit the model's applicability. The model would not be suitable for simulating the effects of loads beyond the yield strain, which is approximately 6000-6500 $\mu\epsilon$ for trabecular bone, and 7100-7600 $\mu\epsilon$ for cortical bone (239). Also, the linear-elastic assumptions do not capture the degradation of strength and stiffness under repeated loading. Thus, in applications where the loss of bone stiffness is of interest, it would be necessary to incorporate a material damage model. Several studies have implemented material damage into FE models (240–243), but none were for the human metatarsal. Since the properties of bone are site-specific (102), it would be necessary to validate the damage models. This could be done by comparing experimental fatigue life to simulated fatigue life, and by comparing damage patterns.

A limitation of the use of strain gauges for FE model validation was that it could only measure the local strain at discrete locations on the bone surface. As the strain gauges in the present study were all placed in the dorsal mid-diaphysis of each metatarsal, the strains at the other locations of the model may not necessarily be accurate. Full-field measurement methods such as digital image correlation could be used for model validation. For digital image correlation, an image of a test specimen after loading is mapped onto an image of the same test specimen before loading. A transformation field between the two images is calculated by maximizing a correlation coefficient (244). If two cameras are used in stereovision using digital image correlation, three-dimensional images of the bone surface could be generated for the correlation analysis. If these

images are combined with CT or MRI images of the specimen before and after loading to capture internal deformations, then the method is called digital volume correlation (244). A limitation of both digital image correlation and digital volume correlation is the continuum assumption associated with these methods. That is, if there are strong discontinuities of the specimens, typically caused by cracks, then the methods fail (244). Furthermore, MRI and CT images could be subject to noise which could affect the analysis for digital volume correlation (244,245).

Although the boundary and loading conditions of the FE model were digitized to match those of the experimental setup, the experimental conditions may not be an accurate depiction of *in vivo* loading. In studies where the model is used to investigate interventions to minimize metatarsal strain, accurate boundary and loading conditions are required. Stokes et al. (246) developed a method to estimate the forces on the metatarsal bones, the metatarsophalangeal joint, and the tension in some of the attached muscles and ligaments using the force distribution underneath the foot. Boundary conditions were estimated using radiographs of the foot (246). Although such a model may be suitable for some of the metatarsals, it does not account for torsion, which is significant during the stance phase of gait in the fifth metatarsal (247). Thus, it may be necessary to develop a more accurate model that incorporates different loading conditions on the metatarsals. Such a model could be used to examine the effects of different footwear, running patterns, and running terrains on metatarsal strains.

The optimization methods used in this study could be applicable to smaller bones, for which empirical density-elasticity equations are difficult to develop, but may not be practical for more complex models which require more computational time to solve. The optimization process could potentially be accelerated through the use of neural networks. Neural networks could be trained to predict values such as the RMSE based on previous results, so they could potentially reduce the number of models to be solved in a given optimization (196).

4.3 Future Directions

Future studies could be used to further investigate the effect of stressed volume on the fatigue life of bone. As explained in Section 2.8.4, stressed volume is a possible explanation of the shorter fatigue lives of larger bone samples (153,154). This hypothesis has not been verified at the whole bone level, but could explain why standardized bone samples do not exhibit fatigue fractures (205,248). In order to verify this concept of stressed volume, fatigue tests at physiological strain magnitude would be performed on cadaveric metatarsals. The stressed volume of each bone would be quantified by using the strain distribution histogram, which would be based on the FE-predicted strains. The relationship between the stressed volume and the experimental fatigue life could then be determined.

The validated FE models could also be used to investigate surgical interventions to treat proximal fifth metatarsal fractures, which include stress fractures, avulsion fractures, and

Jones fractures. The type of fifth metatarsal fracture is typically classified based on the location of the fracture (249). In many cases, surgical intervention is required to assist the alignment and fracture healing of fifth metatarsals. Possible complications from the surgical intervention include the continued nonunion of the bone, as well as the fracture of the surgical screw (250). Although the FE model cannot simulate fracture healing to prevent nonunion, FE models derived from a patient's CT scans could potentially be used to determine the optimal screw design and positioning. Different loads representing different foot postures or activities could be applied to the models to evaluate the factor of safety and stability of surgical interventions, which could aid decision-making. Similar approaches could be used for metatarsal osteosynthesis operations after osteotomy interventions for hallux valgus (164,251).

Furthermore, the FE metatarsal models could be incorporated into FE models of the entire foot to evaluate the risk of stress fractures or acute metatarsal injuries. Such models could potentially provide more accurate boundary conditions for the metatarsals. An advantage of having foot models is that the effect of foot shape, muscles, ligaments, and soft tissues would be captured. However, the inclusion of the additional structures and their interactions requires validation studies to be performed on the models of the structures.

As mentioned in the previous section, the FE models could be used to investigate different interventions to minimize metatarsal strain and fracture risk. Such studies would examine different footwear, running patterns, and running surfaces. For each of the

different conditions, forces would be recorded using plantar pressure recordings and used as input to an appropriate musculoskeletal model, which would find the input forces for the FE model. Fracture risk would then be calculated using an appropriate probabilistic model. An example of such a model is the Weibull model developed by Taylor and Kuiper (252), which accounts for the strain range and the stressed volume.

Future studies should also combine the FE model with the damage model, which was described in the previous section. Repetitive loading scenarios could be applied to the FE models to estimate injury risk. In addition, the load magnitudes and directions could be varied between cycles to simulate different activities such as sprinting, jumping, and cutting. Such variable loading scenarios are relevant in sports such as soccer and basketball. The frequencies of such maneuvers could be captured by placing accelerometers or GPS systems on athletes during a training session or a match. Force plates or plantar pressure recording devices could then be used to measure the forces involved in such maneuvers. With an appropriate musculoskeletal model, the forces could be converted to force inputs into the FE models to estimate injury risk. The results could potentially be used by coaches or athletes to control playing time in order to prevent metatarsal stress fractures.

4.4 Final Remarks

This study verified and validated a finite element modeling routine for the human metatarsal. Using a combined numerical-experimental study in which strain gauge

measurements from mechanical tests were directly compared with strain predictions from FE models, it was found that optimizing the density-elasticity relationships improve the accuracy of the FE predictions. This validated FE model could be used to further elucidate the mechanisms underlying stress fractures. The model could also be used to evaluate surgical interventions for metatarsals, as well as to evaluate potential interventions to minimize metatarsal strain. An incorporation of the present model with a damage model would further expand the potential of the FE model to be used as a tool to predict fracture risk and prevent metatarsal stress fractures in sport.

References

1. Matheson GO, Clement DB, McKenzie DC, Taunton JE, Lloyd-Smith DR, MacIntyre JG. Stress fractures in athletes. A study of 320 cases. *Am J Sports Med.* 1987;15(1):46–58.
2. Milgrom C, Giladi M, Stein M, Kashtan H, Margulies J, Chisin R, et al. Stress fractures in military recruits. A prospective study showing an unusually high incidence. *J Bone Jt Surgery Br Vol.* 1985;67–B(5):732–5.
3. Harrast MA, Colonna D. *Stress Fractures in Runners.* Clin Sports Med. Elsevier Ltd; 2010;29(3):399–416.
4. Carter DR, Caler WE, Spengler DM, Frankel VH. Fatigue behavior of adult cortical bone: the influence of mean strain and strain range. *Acta Orthop Scand.* 1981;52(5):481–90.
5. Milgrom C, Finestone A, Sharkey N, Hamel A, Mandes V, Burr D, et al. Metatarsal strains are sufficient to cause fatigue fracture during cyclic overloading. *Foot Ankle Int.* 2002;23(3):230–5.
6. Arndt A, Westblad P, Ekenman I, Lundberg A. A comparison of external plantar loading and in vivo local metatarsal deformation wearing two different military boots. *Gait Posture.* 2003;18(2):20–6.
7. Arndt A, Ekenman I, Westblad P, Lundberg A. Effects of fatigue and load variation on metatarsal deformation measured in vivo during barefoot walking. *J Biomech.* 2002;35(5):621–8.
8. Varghese B, Short D, Penmetsa R, Goswami T, Hangartner T. Computed-tomography-based finite-element models of long bones can accurately capture

- strain response to bending and torsion. *J Biomech.* Elsevier; 2011;44(7):1374–9.
9. Schileo E, Taddei F, Malandrino A, Cristofolini L, Viceconti M. Subject-specific finite element models can accurately predict strain levels in long bones. *J Biomech.* 2007;40(13):2982–9.
 10. Bennell K, Matheson G, Meeuwisse W, Brukner P. Risk factors for stress fractures. *Sport Med.* 1999;28(2):91–122.
 11. Jones BH, Harris JM, Vinh TN, Rubin C. Exercise-Induced Stress Fractures and Stress Reactions of Bone: Epidemiology, Etiology, and Classification. *Exerc Sport Sci Rev.* 1989;17(1):379–422.
 12. Brunet ME, Cook SD, Brinker MR, Dickinson JA. A survey of running injuries in 1505 competitive and recreational runners. *J Sports Med Phys Fitness.* 1990;30(3):307–15.
 13. Rudzki SJ. Injuries in Australian Army recruits. Part I: Decreased incidence and severity of injury seen with reduced running distance. *Mil Med.* 1997;162(7):472–6.
 14. Popovich RM, Gardner JW, Potter R, Knapik JJ, Jones BH. Effect of rest from running on overuse injuries in Army basic training. *Am J Prev Med.* 2000;18(3S):147–55.
 15. Ekstrand J, Torstveit MK. Stress fractures in elite male football players. *Scand J Med Sci Sport.* 2012;22(3):341–6.
 16. Pepper M, Akuthota V, McCarty EC. The pathophysiology of stress fractures. *Clin Sports Med.* 2006;25(1):1–16.
 17. Warden SJ, Burr DB, Brukner PD. Stress Fractures : Pathophysiology,

- Epidemiology, and Risk Factors. *Curr Osteoporos Rep.* 2006;4(3):103–9.
18. Walter SD, Hart LE, McIntosh JM, Sutton JR. The Ontario Cohort Study of Running-Related Injuries. *Arch Intern Med.* 1989;149(11):2561–4.
 19. Marti B, Vader JP, Minder CE, Abelin T. On the epidemiology of running injuries. The 1984 Bern Grand-Prix study. *Am J Sports Med.* 1988;16(3):285–94.
 20. Macera CA, Pate RR, Powell KE, Jackson KL, Kendrick JS, Craven TE. Predicting lower-extremity injuries among habitual runners. *Arch Intern Med.* 1989;149(11):2565–8.
 21. Milgrom C, Finestone A, Segev S, Olin C, Arndt T, Ekenman I. Are overground or treadmill runners more likely to sustain tibial stress fracture? *Br J Sports Med.* 2003;37(2):160–3.
 22. Zahger D, Abramovitz A, Zelikovsky L, Israel O, Israel P. Stress fractures in female soldiers: An epidemiological investigation of an outbreak. *Mil Med.* 1988;153(9):448–50.
 23. Sabick MB, Torry MR, Kim Y-K, Hawkins RJ. Humeral Torque in Professional Baseball Pitchers. *Am J Sports Med.* 2004;32(4):892–8.
 24. Lord MJ, Ha KI, Song KS. Stress fractures of the ribs in golfers. *Am J Sports Med.* 1996;24(1):118–22.
 25. Warden SJ, Gutschlag FR, Wajswelner H, Crossley KM. Aetiology of rib stress fractures in rowers. *Sports Med.* 2002;32(13):819–36.
 26. Hickey GJ, Fricker PA, McDonald WA. Injuries to elite rowers over a 10-yr period. *Med Sci Sport Exerc.* 1997;29(12):1567–72.
 27. Beck TJ, Ruff CB, Mourtada FA, Shaffer RA, Maxwell-Williams K, Kao GL, et

- al. Dual-energy X-ray absorptiometry derived structural geometry for stress fracture prediction in male U.S. Marine Corps recruits. *J Bone Miner Res.* 1996;11(5):645–53.
28. Bennell KL, Malcolm SA, Wark JD, Brukner PD. Models for the pathogenesis of stress fractures in athletes. *Br J Sports Med.* 1996;30(3):200–4.
29. Stanitski CL, McMaster JH, Scranton PE. On the nature of stress fractures. *Am J Sports Med.* 1978;6(6):391–6.
30. Voloshin AS, Mizrahi J, Verbitsky O, Isakov E. Dynamic loading on the human musculoskeletal system -- effect of fatigue. *Clin Biomech.* 1998;13(7):515–20.
31. Clement DB. Tibial stress athletes syndrome in athletes. *J Sports Med.* 1974;2(2):81–5.
32. Scott S, Winter DA. Internal forces of chronic running injury sites. *Med Sci Sports Exerc.* 1990;22(3):357–69.
33. Bennell KL, Malcolm SA, Thomas S a, Reid SJ, Brukner PD, Ebeling PR, et al. Risk factors for stress fractures in track and field athletes. A twelve-month prospective study. *Am J Sports Med.* 1996;24(6):810–8.
34. Milgrom C. The Israeli elite infantry recruit: a model for understanding the biomechanics of stress fractures. *J R Coll Surg Edinb.* 1989;34(6 Suppl):S18-22.
35. Kowal DM. The Nature and Causes of Injuries in Female Recruits Resulting from an 8-Week Physical Training Program,. *Am J Sports Med.* 1980;8(4):265–9.
36. Miller GJ, Purkey WW. The geometric properties of paired human tibiae. *J Biomech.* 1980;13(1):1–8.
37. Bell DG, Jacobs I. Electromechanical response times and rate of force

- development in males and females. Vol. 18, *Medicine and Science in Sports and Exercise*. 1986. p. 31–6.
38. Winter EM, Brookes FBC. Electromechanical response times and muscle elasticity in men and women. *Eur J Appl Physiol Occup Physiol*. 1991;63(2):124–8.
 39. Carter DR, Caler WE, Spengler DM, Frankel VH. Uniaxial fatigue of human cortical bone. The influence of tissue physical characteristics. *J Biomech*. 1981;14(7):461–70.
 40. Taylor D, Lee TC. Microdamage and mechanical behaviour: predicting failure and remodelling in compact bone. *J Anat*. 2003;203(2):203–11.
 41. Frusztajer NT, Dhuper S, Warren MP, Brooks-Gunn J, Fox RP. Nutrition and the incidence of stress fractures in ballet dancers. *Am J Clin Nutr*. 1990;51(5):779–83.
 42. Nattiv A, Puffer JC, Green GA. Lifestyles and health risks of collegiate athletes: a multi-center study. Vol. 7, *Clinical journal of sport medicine*. 1997. p. 262–72.
 43. Loucks AB, Horvath SM. Athletic amenorrhea: a review. *Med Sci Sports Exerc*. 1985;17(1):56–75.
 44. Nattiv A, Armsey Jr. TD. Stress injury to bone in the female athlete. *Clin Sport Med*. 1997;16(2):197–224.
 45. Frost HM. A new direction for osteoporosis research: A review and proposal. *Bone*. 1991;12(6):429–37.
 46. Drinkwater BL, Nilson K, Chestnut III CH, Bremner WJ, Shainholtz S, Southworth MB. Bone mineral content of amenorrheic and eumenorrheic athletes. *N Engl J Med*. 1984;311(5):277–81.
 47. MacDougall JD, Webber CE, Martin J, Ormerod S, Chesley A, Younglai E V, et

- al. Relationship among running mileage, bone density, and serum testosterone in male runners. *J Appl Physiol*. 1992;73(3):1165–70.
48. Smith R, Rutherford OM. Spine and total body bone mineral density and serum testosterone levels in male athletes. *Eur J Appl Physiol Occup Physiol*. 1993;67(4):330–4.
49. Gardner LI, Dziados JE, Jones BH, Brundage JF, Harris JM, Sullivan R, et al. Prevention of lower extremity stress fractures: A controlled trial of a shock absorbent insole. *Am J Public Health*. 1988;78(12):1563–7.
50. Cline A, Jansen G, Melby C. Stress fractures in female army recruits: implications of bone density, calcium intake, and exercise. *J Am Coll Nutr*. 1998;17(2):128–35.
51. Martin RB, Burr DB, Sharkey NA, Fyhrie DP. Skeletal tissue mechanics. Vol. 112, *American Journal of Physical Anthropology*. 2015. 435-436 p.
52. Weiner D, Wagner DH. The Material Bone : Structure- Mechanical Function Relations. *Annu Rev Mater Sci*. 1998;28:271–98.
53. Sasaki N, Matsushima N, Ikawa T, Yamamura H, Fukuda A. Orientation of bone mineral and its role in the anisotropic mechanical properties of bone-Transverse anisotropy. *J Biomech*. 1989;22(2):157–64.
54. Weiner S, Traub W. Bone Structure : From Angstroms To Microns. *FASEB J*. 1992;6(3):879–85.
55. Martin AD, McCulloch RG. Bone dynamics: stress, strain and fracture. *J Sports Sci*. 1987;5(2):155–63.
56. Evans FG, Vincentelli R. Relation of collagen fiber orientation to some mechanical properties of cortical bone. *J Biomech*. 1969;2(1):63–71.

57. Vincentelli R, Evans FG. Relations among mechanical properties, collagen fibers, and calcification in adult human cortical bone. *J Biomech.* 1971;4(3):193–201.
58. Einhorn TA. Bone strength: The bottom line. *Calcif Tissue Int.* 1992;51(5):333–9.
59. Evans FG. The mechanical properties of bone. *Clinical Orthopaedics and Related Research.* 1973. 37-48 p.
60. Currey JD. The effects of drying and re-wetting on some mechanical properties of cortical bone. *J Biomech.* 1988;21(5):439–41.
61. Fosse L, Ronningen H, Benum P, Sandven RB. Influence of water and fat content on compressive stiffness properties of impacted morsellized bone - An experimental ex vivo study on bone pellets. *Acta Orthop.* 2006;77(1):15–22.
62. Sasaki N, Enyo A. Viscoelastic properties of bone as a function of water content. *J Biomech.* 1995;28(7):809–15.
63. Burr DB, Schaffler MB, Yang KH, Lukoscsek M, Sivaneri N, Blaha JD, et al. Skeletal change in response to altered strain environments: Is woven bone a response to elevated strain? *Bone.* 1989;10(3):223–33.
64. Currey JD. The many adaptations of bone. *J Biomech.* 2003;36(10):1487–95.
65. Carter DR, Spengler DM. Mechanical properties and composition of cortical bone. *Clin Orthop Relat Res.* 1978;135:192–217.
66. Schaffler MB, Burr DB, Frederickson RG. Morphology of the osteonal cement line in human bone. *Anat Rec.* 1987;217(3):223–8.
67. Evans FG, Bang S. Differences and relationships between the physical properties and the microscopic structure of human femoral, tibial and fibular cortical bone. *Am J Anat.* 1967;120(1):79–88.

68. Dempster WT, Coleman RF. Tensile strength of bone along and across the grain. *J Appl Physiol.* 1961;16(2):355–60.
69. Pope MH, Outwater JO. Mechanical properties of bone as a function of position and orientation. *J Biomech.* 1974;7(1):61–6.
70. Evans FG, Riolo ML. Relations between the Fatigue Life and Histology of Adult Human Cortical Bone. *J Bone Jt Surg.* 1970;52–A(8):1579–86.
71. Miller TL, Kaeding CC. *Stress Fractures in Athletes.* 2015.
72. Lanyon LE. Osteocytes, strain detection, bone modeling and remodeling. *Calcif Tissue Int.* 1993;53(S1):S102–7.
73. Hadjidakis DJ, Androulakis II. Bone remodeling. *Ann N Y Acad Sci.* 2006;1092(1):385–96.
74. Keaveny TM, Morgan EF, Yeh OC. Bone Mechanics. In: *Standard Handbook of Biomedical Engineering and Design.* 2004. p. 8.1-8.23.
75. McCalden RW, Mcgeough A, Barker MB, Court-Brown CM. Age-Related Changes in the Tensile Properties of Cortical Bone. *J Bone Jt Surg.* 1993;75–A(8):1193–205.
76. Wright TM, Hayes WC. Fracture mechanics parameters for compact bone-Effects of density and specimen thickness. *J Biomech.* 1977;10(7):419–30.
77. Bonfield W. Advances in the fracture mechanics of cortical bone. *J Biomech.* 1987;20(11–12):1071–81.
78. Pope MH, Outwater JO. The Fracture Characteristics of Bone Substance. *J Biomech.* 1972;5(5):457–65.
79. Currey JD. Differences in the tensile strength of bone of different histological

- types. *J Anat.* 1959;93(Pt 1):87–95.
80. Currey J. The effects of strain rate, reconstruction and mineral content on some mechanical properties of bovine bone. *J Biomech.* 1975;8(1):81–86.
 81. Carter D, Hayes W. Compact bone fatigue damage. 1. Residual strength and stiffness. *J Biomech.* 1977;10(5–6):325–37.
 82. Carter DR, Hayes WC, Schurman DJ. Fatigue life of compact bone-II. Effects of microstructure and density. *J Biomech.* 1976;9(4):211–8.
 83. Weiner S, Traub W, Wagner HD. Lamellar bone: structure– function relations. *J Struct Biol.* 1999;126(3):241–255.
 84. Krempien B, Geiger G, Ritz E. Structural Changes of Cortical Bone in Secondary Hyperparathyroidism. *Virchows Arch A Path Anat Histol.* 1975;366(3):249–56.
 85. Ascenzi A, Bonucci E. The Tensile Properties of Single Osteons. *Anat Rec.* 1967;158(4):375–86.
 86. Ascenzi A, Bonucci E. The compressive properties of single osteons. *Anat Rec.* 1968;161(3):377–91.
 87. Evans FG, Vincentelli R. Relations of the compressive properties of human cortical bone to histological structure and calcification. *J Biomech.* 1974;7(1):1–10.
 88. Lees S, Davidson CL. The role of collagen in the elastic properties of calcified tissues. *J Biomech.* 1977;10(8):473–86.
 89. Vashishth D, Gibson GJ, Khoury JI, Schaffler MB, Kimura J, Fyhrie DP. Influence of nonenzymatic glycation on biomechanical properties of cortical bone. *Bone.* 2001;28(2):195–201.

90. Wang X, Shen X, Li X, Mauli Agrawal C. Age-related changes in the collagen network and toughness of bone. *Bone*. 2002;31(1):1–7.
91. Behiri JC, Bonfield W. Fracture mechanics of bone-The effects of density, specimen thickness and crack velocity on longitudinal fracture. *J Biomech*. 1984;17(1):25–34.
92. Crowninshield RD, Pope MH. The response of compact bone in tension at various strain rates. *Ann Biomed Eng*. 1974;2(2):217–25.
93. McElhaney JH. Dynamic response of bone and muscle tissue. *J Appl Physiol*. 1966;21(4):1231–6.
94. Wright TM, Hayes WC. Tensile testing of bone over a wide range of strain rates: effects of strain rate, microstructure and density. *Med Biol Eng*. 1976;14(6):671–80.
95. Nalla RK, Kinney JH, Ritchie RO. Mechanistic fracture criteria for the failure of human cortical bone. *Nat Mater*. 2003;2(3):164–8.
96. Griffiths JR, Owen DRJ. An elastic-plastic stress analysis for a notched bar in plane strain bending. *J Mech Phys Solids*. 1971;19(6):419–31.
97. Fondrk MT, Bahniuk EH, Davy DT. A damage model for nonlinear tensile behavior of cortical bone. *J Biomech Eng*. 1999;121(5):533–41.
98. Courtney AC, Hayes WC, Gibson LJ. Age-related differences in post-yield damage in human cortical bone. Experiment and model. *J Biomech*. 1996;29(11):1463–71.
99. Caler WE, Carter DR. Bone Creep-Fatigue Damage Accumulation. *J Biomech*. 1989;22(6/7):625–35.

100. Odgaard A, Hvid I, Linde F. Compressive axial strain distributions in cancellous bone specimens. *J Biomech.* 1989;22(8–9):829–35.
101. Odgaard A, Linde F. The underestimation of Young’s modulus in compressive testing of cancellous bone specimens. *J Biomech.* 1991;24(8):691–8.
102. Morgan EF, Bayraktar HH, Keaveny TM. Trabecular bone modulus-density relationships depend on anatomic site. *J Biomech.* 2003;36(7):897–904.
103. Goldstein SA, Wilson DL, Sonstegard DA, Matthews LS. The mechanical properties of human tibial trabecular bone as a function of metaphyseal location. *J Biomech.* 1983;16(12):965–9.
104. Ciarelli MJ, Goldstein S a, Kuhn JL, Cody DD, Brown MB. Evaluation of orthogonal mechanical properties and density of human trabecular bone from the major metaphyseal regions with materials testing and computed tomography. *J Orthop Res.* 1991;9(5):674–82.
105. Goulet RW, Goldstein SA, Ciarelli MJ, Kuhn JL, Brown MB, Feldkamp LA. The relationship between the structural and orthogonal compression properties of trabecular bone. *J Biomech.* 1994;27(4):375–89.
106. Linde F, Pongsoipetch B, Frich LH, Hvid I. Three-axial strain controlled testing applied to bone specimens from the proximal tibial epiphysis. *J Biomech.* 1990;23(11):1167–72.
107. Townsend PR, Raux P, Rose RM, Miegel RE, Radin EL. The distribution and anisotropy of the stiffness of cancellous bone in the human patella. *J Biomech.* 1975;8(6):363–7.
108. Keaveny TM, Hayes WC. Mechanical properties of cortical and trabecular bone.

- Bone. 1993;7:285–344.
109. Choi K, Goldstein SA. A Comparison of the Fatigue Behavior of Human Trabecular and Cortical Bone Tissue. *J Biomech.* 1992;25(12):1371–81.
 110. Currey JD. Mechanical Properties of Bone. *Clin Orthop Relat Res.* 1970;70:210–30.
 111. Mazess RB. On aging bone loss. *Clin Orthop.* 1982;(165):239–52.
 112. Mosekilde L, Mosekilde L, Danielsen CC. Biomechanical competence of vertebral trabecular bone in relation to ash density and age in normal individuals. *Bone.* 1987;8(2):79–85.
 113. Bergot C, Laval-Jeantet AM, Preteux F, Meunier A. Measurement of anisotropic vertebral trabecular bone loss during aging by quantitative image analysis. *Calcif Tissue Int.* 1988;43(3):143–9.
 114. Mosekilde L. Age-related changes in vertebral trabecular bone architecture—assessed by a new method. *Bone.* 1988;9(4):247–50.
 115. Mosekilde L, Mosekilde L. Sex differences in age-related changes in vertebral body size, density and biomechanical competence in normal individuals. *Bone.* 1990;11(2):67–73.
 116. Prêteux F, Bergot C, Laval-Jeantet AM. Automatic quantification of vertebral cancellous bone remodeling during aging. *Anat Clin.* 1985;7(3):203–8.
 117. Snyder SM, Schneider E. Estimation of mechanical properties of cortical bone by computed tomography. *J Orthop Res.* 1991;9(3):422–31.
 118. Bell GH, Dunbar O, Beck JS, Gibb A. Variations in strength of vertebrae with age and their relation to osteoporosis. *Calcif Tissue Res.* 1967;1(1):75–86.

119. Carter DR, Hayes WC. The Compressive Behaviour of Bone as a Two Phase Porous Structure. *J Bone Jt Surg.* 1977;59-A(7):954–62.
120. Ducheyne P, Heymans L, Martens M, Aernoudt E, de Meester P, Mulier JC. The mechanical behaviour of intracondylar cancellous bone of the femur at different loading rates. *J Biomech.* 1977;10(11–12):747–62.
121. Burr DB, Forwood MR, Fyhrie DP, Martin RB, Schaffler MB, Turner CH. Bone Microdamage and Skeletal Fragility in Osteoporotic and Stress Fractures. *J Bone Miner Res.* 1997;12(1):6–15.
122. Burr DB, Martin RB, Schaffler MB, Radin EL. Bone remodeling in response to in vivo fatigue microdamage. *J Biomech.* 1985;18(3):189–200.
123. Mori S, Burr DB. Increased intracortical remodeling following fatigue damage. *Bone.* 1993;14(2):103–9.
124. Wang Z, Norman TL. Microdamage of human cortical bone: Incidence and morphology in long bones. *Bone.* 1997;20(4):375–9.
125. Vashishth D, Koontz J, Qiu SJ, Lundin-Cannon D, Yeni YN, Schaffler MB, et al. In vivo diffuse damage in human vertebral trabecular bone. *Bone.* 2000;26(2):147–52.
126. Wenzel TE, Schaffler MB, Fyhrie DP. In vivo trabecular microcracks in human vertebral bone. *Bone.* 1996;19(2):89–95.
127. Burr DB, Stafford T. Validity of the bulk-staining technique to separate artifactual from in vivo bone microdamage. *Clinical Orthopaedics and Related Research.* 1990. p. 305–8.
128. Schaffler MB, Choi K, Milgrom C. Aging and matrix microdamage accumulation

- in human compact bone. *Bone*. 1995;17(6):521–5.
129. Taylor D, Lee TC. Measuring the shape and size of microcracks in bone. *J Biomech*. 1998;31(12):1177–80.
 130. Taylor D, Hazenberg JG, Lee TC. Living with cracks: damage and repair in human bone. *Nat Mater*. 2007;6(4):263–8.
 131. Martin RB. Targeted bone remodeling involves BMU steering as well as activation. *Bone*. 2007;40(6):1574–80.
 132. Martin RB. Is all cortical bone remodeling initiated by microdamage? *Bone*. 2002;30(1):8–13.
 133. Parfitt AM. Targeted and nontargeted bone remodeling: Relationship to basic multicellular unit origination and progression. *Bone*. 2002;30(1):5–7.
 134. Burr DB. Targeted and Nontargeted Remodeling. *Bone*. 2002;30(1):2–4.
 135. Bentolila V, Boyce TM, Fyhrie DP, Drumb R, Skerry TM, Schaffler MB. Intracortical remodeling in adult rat long bones after fatigue loading. *Bone*. 1998;23(3):275–81.
 136. Weller A, Harner CD, Hogan M V, Miller TL, Kaeding CC, Heckman JD, et al. Stress Fractures in Athletes. 2015;
 137. Murguia MJ, Vailas A, Mandelbaum B, Norton J, Hodgdon J, Goforth H, et al. Elevated plasma hydroxyproline: A possible risk factor associated with connective tissue injuries during overuse. *Am J Sport Med*. 1988;16(6):660–4.
 138. Roub LW, Gumerman LW, Hanley EN, Clark MW, Goodman M, Herbert DL. Bone stress: a radionuclide imaging perspective. *Radiology*. 1979;132(2):431–8.
 139. Li GP, Zhang SD, Chen G, Chen H, Wang a M. Radiographic and histologic

- analyses of stress fracture in rabbit tibias. *Am J Sports Med.* 1985;13(5):285–94.
140. Burrows HJ. Fatigue infraction of the middle of the tibia in ballet dancers. *J bone Jt Surg.* 1956;38 B(1):83–94.
141. Arangio GA, Xiao D, Salathe EP. Biomechanical study of stress in the fifth metatarsal. *Clin Biomech.* 1997;12(3):160–4.
142. Arangio GA, Beam H, Kowalczyk G, Salathe EP. Analysis of stress in the metatarsals. *Foot Ankle Surg.* 1998;4(3):123–8.
143. Ekstrand J, van Dijk CN. Fifth metatarsal fractures among male professional footballers: a potential career-ending disease. *Br J Sports Med.* 2013;47(12):754–8.
144. Ekstrand J. Playing too many matches is negative for both performance and player availability - Results from the on-going UEFA injury study. *Dtsch Z Sport.* 2013;64(1):5–9.
145. Caler WE, Carter DR, Harris WH. Techniques for implementing an in vivo bone strain gage system. *J Biomech.* 1981;14(7):503–7.
146. Yang PF, Brüggemann GP, Rittweger J. What do we currently know from in vivo bone strain measurements in humans? *J Musculoskelet Neuronal Interact.* 2011;11(1):8–20.
147. Lanyon LE, Hampson WG, Goodship a E, Shah JS. Bone deformation recorded in vivo from strain gauges attached to the human tibial shaft. *Acta Orthop Scand.* 1975;46(2):256–68.
148. Burr DB, Milgrom C, Fyhrie D, Forwood M, Nyska M, Finestone A, et al. In vivo measurement of human tibial strains during vigorous activity. *Bone.*

- 1996;18(5):405–10.
149. Milgrom C, Burr D, Fyhrie D, Forwood M, Finestone A, Nyska M, et al. The effect of shoe gear on human tibial strains recorded during dynamic loading: a pilot study. *Foot Ankle Int.* 1996;17(11):667–71.
 150. Rolf C, Westblad P, Ekenman I, Lundberg A, Murphy N, Lamontagne M, et al. An experimental in vivo method for analysis of local deformation on tibia, with simultaneous measures of ground reaction forces, lower extremity muscle activity and joint motion. *Scand J Med Sci Sports.* 1997;7(3):144–51.
 151. Milgrom C, Simkin A, Eldad A, Nyska M, Finestone A. Using bone’s adaptation ability to lower the incidence of stress fractures. *Am J Sports Med.* 2000;28(2):245–51.
 152. Milgrom C, Finestone A, Levi Y, Simkin A, Ekenman I, Mendelson S, et al. Do high impact exercises produce higher tibial strains than running? *Br J Sports Med.* 2000;34(3):195–9.
 153. Taylor D. Fatigue of bone and bones: An analysis based on stressed volume. *J Orthop Res.* 1998;16(2):163–9.
 154. Taylor D, O’Brien F, Prina-Mello A, Ryan C, O’Reilly P, Lee TC. Compression data on bovine bone confirms that a “stressed volume” principle explains the variability of fatigue strength results. *J Biomech.* 1999;32(11):1199–203.
 155. Brekelmans WA, Poort HW, Slooff TJ. A New Method to Analyse the Mechanical Behaviour of Skeletal Parts. *Acta Orthop Scand Scand.* 1972;43(5):301–17.
 156. Harrigan TP, Jasty M, Mann RW, Harris WH. Limitations of the continuum assumption in cancellous bone. *J Biomech.* 1988;21(4):269–75.

157. Huiskes R, Chao EYS. A survey of finite element analysis in orthopedic biomechanics: The first decade. *J Biomech.* 1983;16(6):385–409.
158. Huiskes R. The various stress patterns of press-fit, ingrown, and cemented femoral stems. *Clin Orthop Relat Res.* 1990;(261):27–38.
159. Vasu R, Carter DR, Harris WH. Stress distributions in the acetabular region-I. Before and after total joint replacement. *J Biomech.* 1982;15(3):155–7.
160. Vasu R, Carter DR, Schurman DJ, Beaupre GS. Epiphyseal-based designs for tibial plateau components-I. Stress analysis in the frontal plane. *J Biomech.* 1986;19(8):647–62.
161. Taylor M, Prendergast PJ. Four decades of finite element analysis of orthopaedic devices: Where are we now and what are the opportunities? *J Biomech.* Elsevier; 2015;48(5):767–78.
162. Pankaj P. Patient-specific modelling of bone and bone-implant systems: The challenges. Vol. 29, *International Journal for Numerical Methods in Biomedical Engineering.* 2013. p. 233–49.
163. Yosibash Z, Nir Trabelsi. Reliable Patient-Specific Simulations of the Femur. In: *Stud Mechanobiol Tissue Eng Biomater.* 2011. p. 3–26.
164. Trabelsi N, Milgrom C, Yosibash Z. Patient-specific FE analyses of metatarsal bones with inhomogeneous isotropic material properties. *J Mech Behav Biomed Mater.* Elsevier; 2014;29:177–89.
165. Yosibash Z, Padan R, Joskowicz L, Milgrom C. A CT-based high-order finite element analysis of the human proximal femur compared to in-vitro experiments. *J Biomech Eng.* 2007;129(3):297–309.

166. Bosisio MR, Talmant M, Skalli W, Laugier P, Mitton D. Apparent Young's modulus of human radius using inverse finite-element method. *J Biomech.* 2007;40(9):2022–8.
167. Gröning F, Bright JA, Fagan MJ, O'Higgins P. Improving the validation of finite element models with quantitative full-field strain comparisons. *J Biomech.* 2012;45(8):1498–506.
168. Moore SM, Ellis B, Weiss JA, McMahon PJ, Debski RE. The glenohumeral capsule should be evaluated as a sheet of fibrous tissue: A validated finite element model. *Ann Biomed Eng.* 2010;38(1):66–76.
169. Lotz JC, Cheal EJ, Hayes WC. Fracture Prediction for the Proximal Femur Using Finite Element Models : Part II — Nonlinear Analysis. *J Biomech Eng.* 1991;113(4):361–5.
170. Kazembakhshi S, Luo Y. Constructing anisotropic finite element model of bone from computed tomography (CT). *Biomed Mater Eng.* 2014;24(6):2619–26.
171. Weinans H, Huiskes R, Grootenboer HJ. Effects of Fit and Bonding Characteristics of Femoral Stems on Adaptive Bone Remodeling. *J Biomech Eng.* 1994;116(4):393–400.
172. Weinans H, Huiskes R, Grootenboer HJ. Trends of mechanical consequences and modeling of a fibrous membrane around femoral hip prostheses. *J Biomech.* 1990;23(10):991–1000.
173. Mihalko WM, Beaudoin AJ, Cardea JA, Krause WR. Finite-element modelling of femoral shaft fracture fixation techniques post total hip arthroplasty. *J Biomech.* 1992;25(5):469–76.

174. Yosibash Z, Tal D, Trabelsi N. Predicting the yield of the proximal femur using high-order finite-element analysis with inhomogeneous orthotropic material properties. *Philos Trans A Math Phys Eng Sci.* 2010;368(1920):2707–23.
175. Hölzer A, Schröder C, Woiczinski M, Sadoghi P, Scharpf A, Heimkes B, et al. Subject-specific finite element simulation of the human femur considering inhomogeneous material properties: A straightforward method and convergence study. *Comput Methods Programs Biomed.* Elsevier Ireland Ltd; 2013;110(1):82–8.
176. Yosibash Z, Trabelsi N, Milgrom C. Reliable simulations of the human proximal femur by high-order finite element analysis validated by experimental observations. *J Biomech.* 2007;40(16):3688–99.
177. Eberle S, Göttliger M, Augat P. An investigation to determine if a single validated density-elasticity relationship can be used for subject specific finite element analyses of human long bones. *Med Eng Phys.* Institute of Physics and Engineering in Medicine; 2013;35(7):875–83.
178. Nazemi SM, Amini M, Kontulainen SA, Milner JS, Holdsworth DW, Masri BA, et al. Prediction of local proximal tibial subchondral bone structural stiffness using subject-specific finite element modeling: Effect of selected density-modulus relationship. *Clin Biomech.* Elsevier Ltd; 2015;30(7):703–12.
179. Austman RL, Milner JS, Holdsworth DW, Dunning CE. The effect of the density-modulus relationship selected to apply material properties in a finite element model of long bone. *J Biomech.* 2008;41(15):3171–6.
180. Taddei F, Cristofolini L, Martelli S, Gill HS, Viceconti M. Subject-specific finite

- element models of long bones: An in vitro evaluation of the overall accuracy. *J Biomech.* 2006;39(13):2457–67.
181. Lotz JC, Gerhart TN, Hayes WC. Mechanical Properties of Trabecular Bone from the Proximal Femur: A Quantitative CT Study. Vol. 14, *Journal of Computer Assisted Tomography.* 1990. p. 107–11.
 182. Lotz JC, Gerhart TN, Hayes WC. Mechanical properties of metaphyseal bone in the proximal femur. *J Biomech.* 1991;24(5):317–29.
 183. Keller TS. Predicting the compressive mechanical behavior of bone. *J Biomech.* 1994;27(9):1159–68.
 184. Li B, Aspden RM. Composition and mechanical properties of cancellous bone from the femoral head of patients with osteoporosis or osteoarthritis. *J Bone Miner Res.* 1997;12(4):641–51.
 185. Ciarelli TE, Fyhrie DP, Schaffler MB, Goldstein S a. Variations in three-dimensional cancellous bone architecture of the proximal femur in female hip fractures and in controls. *J Bone Miner Res.* 2000;15(1):32–40.
 186. Linde F, Hvid I, Madsen F. The effect of specimen geometry on the mechanical behaviour of trabecular bone specimens. *J Biomech.* 1992;25(4):359–68.
 187. Rho JY, Hobatho MC, Ashman RB. Relations of mechanical properties to density and CT numbers in human bone. *Med Eng Phys.* 1995;17(5):347–55.
 188. Keyak JH, Lee IY, Skinner HB. Correlations between orthogonal mechanical properties and density of trabecular bone: Use of different densitometric measures. *J Biomed Mater Res.* 1994;28(11):1329–36.
 189. Dalstra M, Huiskes R, Odgaard A, van Erning L. Mechanical and textural

- properties of pelvic trabecular bone. *J Biomech.* 1993;26(4–5):523–35.
190. Keaveny TM, Pinilla TP, Crawford RP, Kopperdahl DL, Lou A. Systematic and random errors in compression testing of trabecular bone. *J Orthop Res.* 1997;15(1):101–10.
191. Ouyang J, Yang GT, Wu WZ, Zhu Q a, Zhong SZ. Biomechanical characteristics of human trabecular bone. *Clin Biomech.* 1997;12(7–8):522–4.
192. Kopperdahl DL, Keaveny TM. Yield strain behavior of trabecular bone. *J Biomech.* 1998;31(7):601–8.
193. Rice JC, Cowin SC, Bowman JA. On the dependence of the elasticity and strength of cancellous bone on apparent density. *J Biomech.* 1988;21(2):155–68.
194. Eberle S, Göttinger M, Augat P. Individual density-elasticity relationships improve accuracy of subject-specific finite element models of human femurs. *J Biomech. Elsevier;* 2013;46(13):2152–7.
195. Cong A, Buijs JO Den, Dragomir-Daescu D. In situ parameter identification of optimal density-elastic modulus relationships in subject-specific finite element models of the proximal femur. *Med Eng Phys. Institute of Physics and Engineering in Medicine;* 2011;33(2):164–73.
196. Nazemi SM, Amini M, Kontulainen SA, Milner JS, Holdsworth DW, Masri BA, et al. Optimizing finite element predictions of local subchondral bone structural stiffness using neural network-derived density-modulus relationships for proximal tibial subchondral cortical and trabecular bone. *Clin Biomech. Elsevier Ltd;* 2017;41(1):1–8.
197. Austman RL, Milner JS, Holdsworth DW, Dunning CE. Development of a

- customized density–modulus relationship for use in subject-specific finite element models of the ulna. *Proc Inst Mech Eng Part H J Eng Med.* 2009;223(6):787–94.
198. ASME. *Guide for Verification and Validation in Computational Solid Mechanics.* Am Soc Mech Eng. 2006;(March):1–53.
199. MacNeil JAM, Adachi JD, Goltzman D, Josse RG, Kovacs CS, Prior JC, et al. Predicting fracture using 2D finite element modelling. *Med Eng Phys. Institute of Physics and Engineering in Medicine;* 2012;34(4):478–84.
200. Toga AW, Thompson PM. Three-dimensional microimaging (MR μ l and μ CT), finite element modeling, and rapid prototyping provide unique insights into bone architecture in osteoporosis. *Anat Rec.* 2001;265(2):101–10.
201. Keyak JH, Skinner HB. Three-dimensional finite element modelling of bone: effects of element size. *J Biomed Eng.* 1992;14(6):483–9.
202. Anderson A, Ellis B, Weiss J. Verification, validation and sensitivity studies in computational biomechanics. *Comput Methods Biomech Biomed Engin.* 2007;10(3):171–84.
203. Almeida SA, Williams KM, Shaffer RA, Luz JT, Badong E, Brodine SK. A physical training program to reduce musculoskeletal injuries in US Marine Corps recruits. Nav Heal Res Center, Tech Report Natl Tech Inf Serv US Dept Commer. 1997;NHRC97-2B.
204. Gross TS, Bunch RP. A mechanical model of metatarsal stress fracture during distance running. *Am J Sports Med.* 1989;17(5):669–74.
205. Schaffler MB, Radin EL, Burr DB. Mechanical and morphological effects of strain rate on fatigue of compact bone. *Bone.* 1989;10(3):207–14.

206. Gutekunst DJ, Patel TK, Smith KE, Commean PK, Silva MJ, Sinacore DR. Predicting ex vivo failure loads in human metatarsals using bone strength indices derived from volumetric quantitative computed tomography. *J Biomech.* Elsevier; 2013;46(4):745–50.
207. Zysset PK, Edward Guo X, Edward Hoffler C, Moore KE, Goldstein SA. Elastic modulus and hardness of cortical and trabecular bone lamellae measured by nanoindentation in the human femur. *J Biomech.* 1999;32(10):1005–12.
208. Wirtz DC, Schiffers N, Pandorf T, Radermacher K, Weichert D, Forst R. Critical evaluation of known bone material properties to realize anisotropic FE-simulation of the proximal femur. *J Biomech.* 2000;33(10):1325–30.
209. Gray HA, Taddei F, Zavatsky AB, Cristofolini L, Gill HS. Experimental validation of a finite element model of a human cadaveric tibia. *J Biomech Eng.* 2008;130(3):31016.
210. Nelder JA, Mead R. A simplex method for function minimization. *Comput J.* 1964;7(4):308–13.
211. Lagarias JC, Reeds JA, Wright MH, Wright PE. Convergence Properties of the Nelder-Mead Simplex Method in Low Dimensions. *SIAM J Optim.* 1998;9(1):112–47.
212. Helgason B, Perilli E, Schileo E, Taddei F, Brynjólfsson S, Viceconti M. Mathematical relationships between bone density and mechanical properties: A literature review. *Clin Biomech.* 2008;23(2):135–46.
213. Ashman RB, Cowin SC, Van Buskirk WC, Rice JC. A continuous wave technique for the measurement of the elastic properties of cortical bone. *J Biomech.*

- 1984;17(5):349–61.
214. Reilly DT, Burstein AH, Frankel VH. The elastic modulus for bone. *J Biomech.* 1974;7(3):271–5.
215. Li B, Aspden RM. Mechanical and material properties of the subchondral bone plate from the femoral head of patients with osteoarthritis or osteoporosis. *Ann Rheum Dis.* 1997;56(4):247–54.
216. Barker DS, Netherway DJ, Krishnan J, Hearn TC. Validation of a finite element model of the human metacarpal. *Med Eng Phys.* 2005;27(2):103–13.
217. Trabelsi N, Yosibash Z, Wutte C, Augat P, Eberle S. Patient-specific finite element analysis of the human femur-A double-blinded biomechanical validation. *J Biomech.* Elsevier; 2011;44(9):1666–72.
218. Zysset PK, Goulet RW, Hollister SJ. A Global Relationship between Trabecular Bone Morphology and Homogenized Elastic Properties. *J Biomech Eng.* 1998;120(5):640–6.
219. Matsuura M, Eckstein F, Lochmüller EM, Zysset PK. The role of fabric in the quasi-static compressive mechanical properties of human trabecular bone from various anatomical locations. *Biomech Model Mechanobiol.* 2008;7(1):27–42.
220. Hodgskinson R, Currey JD. Young's modulus, density and material properties in cancellous bone over a large density range. *J Mater Sci Mater Med.* 1992;3(5):377–81.
221. Rho JY. An ultrasonic method for measuring the elastic properties of human tibial cortical and cancellous bone. *Ultrasonics.* 1996;34(8):777–83.
222. Boskey AL, Coleman R. Aging and Bone. *J Dent Res.* 2010;89(12):1333–48.

223. Pakdel A, Robert N, Fialkov J, Maloul A, Whyne C. Generalized method for computation of true thickness and x-ray intensity information in highly blurred sub-millimeter bone features in clinical CT images. *Phys Med Biol*. 2012;57(23):8099–116.
224. Peng L, Bai J, Zeng X, Zhou Y. Comparison of isotropic and orthotropic material property assignments on femoral finite element models under two loading conditions. *Med Eng Phys*. 2006;28(3):227–33.
225. Trabelsi N, Yosibash Z. Patient-specific finite-element analyses of the proximal femur with orthotropic material properties validated by experiments. *J Biomech Eng*. 2011;133(6):61001.
226. Baca V, Horak Z, Mikulenka P, Dzupa V. Comparison of an inhomogeneous orthotropic and isotropic material models used for FE analyses. *Med Eng Phys*. 2008;30(7):924–30.
227. Yang H, Ma X, Guo T. Some factors that affect the comparison between isotropic and orthotropic inhomogeneous finite element material models of femur. *Med Eng Phys*. Institute of Physics and Engineering in Medicine; 2010;32(6):553–60.
228. Reilly DT, Burstein AH. The elastic and ultimate properties of compact bone tissue. *J Biomech*. 1975;8(6):393–405.
229. Knets I V. *Mechanics of Biological Tissues: A Review*. *Polym Mech*. 1977;13(3):434–41.
230. Turner CH, Burr DB. *Basic Biomechanical Measurements of Bone : A Tutorial*. *Bone*. 1993;14(4):595–608.
231. Whitehouse WJ. The quantitative morphology of anisotropic trabecular bone. *J*

- Microsc. 1974;101(2):153–68.
232. Whitehouse WJ. A stereological method for calculating internal surface areas in structures which have become anisotropic as the result of linear expansions or contractions. *J Microsc.* 1974;101(2):169–76.
233. Cowin SC. The relationship between the elasticity tensor and the fabric tensor. *Mech Mater.* 1985;4(2):137–47.
234. Kuhn JL, Goldstein SA, Feldcamp LA, Goulet RW, Jesion G. Evaluation of a Microcomputed Tomography System to Study Trabecular Bone Structure. *J Orthop Res.* 1990;8(6):833–42.
235. Kinney JH, Lane NE, Haupt DL. In Vivo , Three-Dimensional Microscopy of Trabecular Bone. *J Bone Miner Res.* 1995;10(2):264–70.
236. Rügsegger P, Koller B, Müller R. A Microtomographic System for the Nondestructive Evaluation of Bone Architecture. *Calcif Tissue Int.* 1996;58(1):24–9.
237. Majumdar S, Kothari M, Augat P, Newitt DC, Link TM, Lin JC, et al. High-Resolution Magnetic Resonance Imaging : Three-Dimensional Trabecular Bone Architecture and Biomechanical Properties. *Bone.* 1998;22(5):445–54.
238. Hipp JA, Jansujwicz A, Simmons CA, Snyder BD. Trabecular Bone Morphology from Micro-Magnetic Resonance Imaging. *J Bone Miner Res.* 1996;11(2):286–92.
239. Bayraktar HH, Morgan EF, Niebur GL, Morris GE, Wong EK, Keaveny TM. Comparison of the elastic and yield properties of human femoral trabecular and cortical bone tissue. *J Biomech.* 2004;37(1):27–35.
240. Cotton J, Zioupos P, Taylor M, Science B, Sciences M. Simulation of material

- property evolution of cortical bone in fatigue bending and its implications on cancellous bone. 1999;1–2.
241. Taylor M, Verdonschot N, Zioupos P, Huiskes R, Zioupos P. A combined finite element method and continuum damage mechanics approach to simulate the in vitro fatigue behavior of human cortical bone. *J Mater Sci Mater Med*. 1999;10(12):841–6.
242. Kosmopoulos V, Keller TS. Finite element modeling of trabecular bone damage. *Comput Methods Biomech Biomed Engin*. 2003;6(3):209–16.
243. Hambli R, Frikha S, Toumi H, Tavares JMRS. Finite element prediction of fatigue damage growth in cancellous bone. *Comput Methods Biomech Biomed Engin*. 2016;19(5):563–70.
244. Grassi L, Isaksson H. Extracting accurate strain measurements in bone mechanics: A critical review of current methods. *J Mech Behav Biomed Mater*. Elsevier; 2015;50:43–54.
245. Dall’Ara E, Barber D, Viceconti M. About the inevitable compromise between spatial resolution and accuracy of strain measurement for bone tissue: A 3D zero-strain study. *J Biomech*. Elsevier; 2014;47(12):2956–63.
246. Stokes IAF, Hutton WC, Stott JR. Forces acting on the metatarsals during normal walking. *J Anat*. 1979;129(3):579–90.
247. Vertullo CJ, Glisson RR, Nunley JA. Torsional Strains in the Proximal Fifth Metatarsal : Implications for Jones and Stress Fracture Management. *Foot Ankle Int*. 2004;25(9):650–6.
248. Schaffler MB, Radin EL, Burr DB. Long-term fatigue behavior of compact bone at

- low strain magnitude and rate. *Bone*. 1990;11(5):321–6.
249. Torg JS, Balduini FC, Zelko RR, Pavlov H, Peff TC, Das M. Fractures of the base of the fifth metatarsal distal to the tuberosity. Classification and guidelines for non-surgical and surgical management. *J Bone Joint Surg Am*. 1984;66(2):209–14.
250. Murawski CD, Kennedy JG. Percutaneous internal fixation of proximal fifth metatarsal jones fractures (Zones II and III) with Charlotte Carolina screw and bone marrow aspirate concentrate: an outcome study in athletes. *Am J Sports Med*. 2011;39(6):1295–301.
251. Kristen KH, Berger K, Berger C, Kampla W, Anzböck W, Weitzel SH. The first metatarsal bone under loading conditions: A finite element analysis. *Foot Ankle Clin N Am*. 2005;10(1):1–14.
252. Taylor D, Kuiper JH. The prediction of stress fractures using a “stressed volume” concept. *J Orthop Res*. 2001;19(5):919–26.

APPENDIX A: CROSS-VALIDATION OF FE-PREDICTED METATARSAL STRAINS SUGGESTS AN INFLUENCE OF AGE AND vBMD ON DENSITY-ELASTICITY RELATIONSHIPS

In Chapter 3, experimentally-measured strains were compared to FE-predicted strains using the published equation (1), $E = 0.51\rho_{app}^{1.37}$. This section takes a closer look at the findings from this comparison.

When the measured strains were plotted against the FE-predicted strains for all bones, the regression line had a slope that was significantly less than 1 (Figure A-1). Further investigation revealed that metatarsals from three of the seven feet had vBMD values that were up to 45% lower than the bones from the remaining four feet. When these bones were separated from the set, the resulting regression equation was an X=Y relationship for the bones with higher vBMD (Figure A-2). For the bones with lower vBMD, the regression equation had a slope that was significantly lower than 1 (Table A-1). The RMSE and the maximum error were also noticeably higher for the bones with lower vBMD (Table A-1).

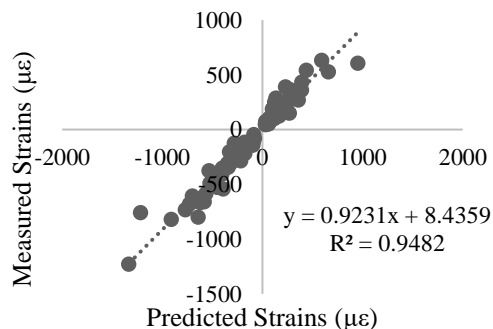


Figure A-1. Measured vs. predicted strains for all metatarsals using the published density-elasticity equation, $E = 0.51\rho_{app}^{1.37}$ (1)

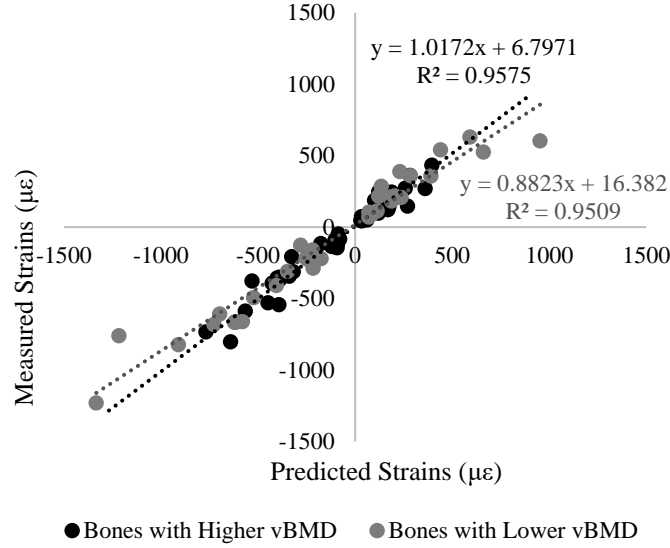


Figure A-2. Measured vs. predicted strains for metatarsals with a higher vBMD (0.40-0.73 g/cm³, black markers), and lower vBMD (0.15-0.34 g/cm³, grey markers) using the published density-elasticity equation, $E = 0.51\rho_{app}^{1.37}$ (1)

Table A-1. Slope, intercept, correlation, R², RMSE in microstrain and as a percentage of the peak measured strain, and maximum error in microstrain and as a percentage of the peak measured strain for different sets of models created using the published density-elasticity equation, $E = 0.51\rho_{app}^{1.37}$ (1)

	All Bones	High vBMD Bones	Low vBMD Bones
Slope	0.92	1.02	0.88
Intercept	8.44	6.80	16.38
R	0.97	0.98	0.98
R²	0.95	0.96	0.95
RMSE (µε)	92.47	63.08	121.39
RMSE (%)	7.51	7.87	9.86
Max Error (µε)	456.32	159.40	456.32
Max Error (%)	37.07	19.89	37.07

The results support the findings of Eberle et al. (2), which stated that the density-elasticity equation varies between different cohorts, such as bones with higher vBMD and lower vBMD. It was observed that elastic moduli at the lower range of densities were higher than the published equation predicted (Figure A-2). These observations could be explained by the findings that lower bone densities (3) and stiffer collagen cross-linking (4) are associated with aging. Since the FE models did not take these changes into account, the models of the bones with lower vBMD behaved too softly, and subsequently resulted in strains that were too high. One way to mitigate this shortcoming would be to use an equation that provides sufficient accuracy for all bones in a given cohort. Such an equation could be developed using optimization techniques which minimize the root mean squared error (RMSE) between measured and predicted strains.

A.1 References

1. Rho JY, Hobatho MC, Ashman RB. Relations of mechanical properties to density and CT numbers in human bone. *Med Eng Phys.* 1995;17(5):347–55.
2. Eberle S, Göttliger M, Augat P. Individual density-elasticity relationships improve accuracy of subject-specific finite element models of human femurs. *J Biomech. Elsevier;* 2013;46(13):2152–7.
3. McCalden RW, Mcgeough A, Barker MB, Court-Brown CM. Age-Related Changes in the Tensile Properties of Cortical Bone. *J Bone Jt Surg.* 1993;75–A(8):1193–205.
4. Wang X, Shen X, Li X, Mauli Agrawal C. Age-related changes in the collagen network and toughness of bone. *Bone.* 2002;31(1):1–7.

APPENDIX B: THE EFFECT OF LOADING ANGLE ON THE VALIDITY OF THE DENSITY-ELASTICITY RELATIONSHIP IN A FINITE ELEMENT MODEL

Chapter 3 describes a finite element model validation study where metatarsals were loaded in an angled cantilever-bending scenario. These metatarsal angles varied depending on the metatarsal (38°, 33°, 30°, 28°, and 24° for the first through fifth metatarsals, respectively), but each metatarsal was positioned at a single angle. However, metatarsals are loaded at a wide range of angles *in vivo* during the stance phase of gait. This prompted a second study to be performed on the second metatarsals of each cadaveric foot, as the second metatarsal is the most prone to stress fractures in runners (1,2).

In this experiment, the metatarsals were positioned at five different angles between 20° and 40° from the horizontal. This was done to examine the influence of loading angle on the accuracy of the density-elasticity equation of the FE model. The study used the same methods as described in Section 3.3, but omitted the optimization of the density-elasticity equations. The material properties for all FE models were assigned using the equation $E = 0.51\rho_{app}^{1.37}$ (3), where E is the elastic modulus in MPa, and ρ_{app} is the apparent density in kg/m³. An additional strain gauge was attached to the plantar surface of each of the second metatarsals. The locations of the plantar strain gauges were identified on the FE models by using scaled photographs. The results of the linear regression between experimentally measured and FE-predicted strains at each metatarsal angle are shown in the table below.

Table B-1. Slope, intercept, correlation, R^2 , RMSE in microstrain and as a percentage of the peak measured strain, and maximum error in microstrain and as a percentage of the peak measured strain for different metatarsal angles relative to the horizontal axis. All models were created using the published density-elasticity equation, $E = 0.51\rho_{app}^{1.37}$ (3)

	20°	25°	30°	35°	40°
Slope	0.77	0.80	0.86	0.86	0.97
Intercept	-1.79	-1.13	-0.13	0.27	2.91
R	0.97	0.97	0.98	0.98	0.98
R²	0.95	0.95	0.96	0.95	0.97
RMSE (μϵ)	116.65	101.37	76.04	71.35	49.00
RMSE (%)	15.76	13.90	10.76	11.27	8.00
Max Error (μϵ)	461.26	415.99	295.00	269.81	129.00
Max Error (%)	62.31	57.05	41.76	42.63	21.07

As shown in Table B-1, the slope of the regression line becomes progressively closer to 1 as the metatarsal angle increases, and the metatarsal becomes more vertical. The RMSE and maximum error also decreases as the metatarsal angle increases.

The results suggest that the published density-elasticity equation is more accurate when there is less bending. When the metatarsals are positioned more horizontally, the model behaves too soft and the FE-predicted strains are higher than the experimentally-measured strains. As applying bending loads in bone causes high strains in the cortical shell, the FE models may be more sensitive to any inaccuracies in the cortical bone region of the density-elasticity relationship. However, as the loading becomes more uniaxial with increased angle, the strains become more evenly distributed over any given

cross-sectional area of the metatarsal, and lower strain gradients result. Consequently, we would hypothesize that the accuracy of the model depends on a larger section of the density-elasticity relationship. Thus, any inaccuracies in one part of the density-elasticity relationship would have a smaller impact on the accuracy of the FE model if the rest of the relationship is accurate. Therefore, models with an applied uniaxial load would be less sensitive to an inaccurate density-elasticity relationship than a model with a bending load.

Another possible explanation for the discrepancy between the models with the different angles is that the cortical bone does not have a separate mesh from the trabecular bone. This could potentially cause both types of bone to be included within a single element. Consequently, the meshing could result in inaccurate density properties of the element, and ultimately an inaccurate elastic modulus. If the model is loaded in a configuration that causes high strain gradients, such as those at the lower angles in Table B-1, then these discrepancies could have a larger effect on the accuracy of the FE model. Further investigation on this property of the mesh could be performed by meshing the cortical and trabecular bone separately by using cortical thickness estimation algorithms similar to those suggested by Pakdel et al. (4). Experiments involving notched specimens could also be performed to examine the influence of the strain gradient on the accuracy of density-elasticity relationships.

In conclusion, the influence of different parts of the density-elasticity relationship varies with different loading conditions of human metatarsals. Loading conditions causing high

strain gradients, such as bending loads, result in a higher sensitivity to the accuracy of the density-elasticity relationships. Therefore, it is important to validate FE models at different loading conditions with differing strain gradients to ensure that the density-elasticity relationships are accurate.

B.1 References

1. Matheson GO, Clement DB, McKenzie DC, Taunton JE, Lloyd-Smith DR, MacIntyre JG. Stress fractures in athletes. A study of 320 cases. *Am J Sports Med.* 1987;15(1):46–58.
2. Milgrom C, Giladi M, Stein M, Kashtan H, Margulies J, Chisin R, et al. Stress fractures in military recruits. A prospective study showing an unusually high incidence. *J Bone Jt Surgery Br Vol.* 1985;67–B(5):732–5.
3. Rho JY, Hobatho MC, Ashman RB. Relations of mechanical properties to density and CT numbers in human bone. *Med Eng Phys.* 1995;17(5):347–55.
4. Pakdel A, Robert N, Fialkov J, Maloul A, Whyne C. Generalized method for computation of true thickness and x-ray intensity information in highly blurred sub-millimeter bone features in clinical CT images. *Phys Med Biol.* 2012;57(23):8099–116.

Appendix C: COPYRIGHT PERMISSIONS

From: Lindsay Loundagin
Sent: Monday, April 17, 2017 11:46 AM
To: Anita Fung
Subject: Co-Author for Anita Fung

I allow Anita Fung to include the manuscript entitled "Experimental Validation of Finite Element Predicted Bone Strain in the Human Metatarsal" in her Master's thesis "Experimental Validation of Finite Element Predicted Bone Strain in the Human Metatarsal"

Lindsay Loundagin

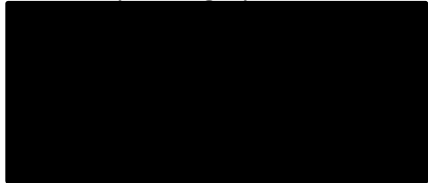
*PhD Kinesiology student
Human Performance Laboratory*



From: Brent Edwards
Sent: Monday, April 17, 2017 11:50 AM
To: Anita Fung
Subject: Co-author Permission

"I allow Anita Fung to include the manuscript entitled "Experimental Validation of Finite Element Predicted Bone Strain in the Human Metatarsal" in her Master's thesis "Experimental Validation of Finite Element Predicted Bone Strain in the Human Metatarsal"."

W. Brent Edwards, Ph.D.
Assistant Professor
Faculty of Kinesiology
University of Calgary



From: Toni Arndt [REDACTED]
Sent: Tuesday, April 18, 2017 12:16 AM
To: Anita Fung
Subject: SV: Permission to Use Copyrighted Material in a Thesis

Dear Anita,

That is no problem at all. I am glad my photo (of my foot ☺) can be useful in your thesis. Would it be possible that you send me a copy of your thesis once it has been published?

Best Regards,

Toni

Från: Anita Fung [REDACTED]
Skickat: den 13 april 2017 22:51
Till: Toni Arndt
Ämne: Re: Permission to Use Copyrighted Material in a Thesis

Dear Dr. Arndt:

I am a University of Calgary graduate student completing my Master's thesis, entitled "Experimental Validation of Finite Element Predicted Bone Strain in the Human Metatarsal".

I would like permission to allow inclusion of the following material in my thesis: Arndt et al. (2002), "Effects of fatigue and load variation on metatarsal deformation measured in vivo during barefoot walking". Specifically, I would like to use Figure 1, "Medial X-ray view of instrumented staple inserted in the second metatarsal". The material will be attributed through a citation.

My published thesis will be added to the institutional repository at the University of Calgary and the Library and Archives Canada. The links for further information about these archives are provided below:

University of Calgary Thesis Repository - The Vault
<http://theses.ucalgary.ca/>

Library and Archives Canada
<http://collectionscanada.gc.ca/>

My proposed publication date is April 24th, 2017. Your review of this request is greatly appreciated.

If you have any questions or concerns, please do not hesitate to contact me.

Thank you in advance for your consideration.

Sincerely,

Anita Fung

MSc. Student

Biomedical Engineering Graduate Program

University of Calgary

